2

(NASA-CR-132304) INVESTIGATION OF LASER HOLOGRAPHIC INTERFEROMETRIC TECHNIQUES FOR STRUCTURE INSPECTION (Old Dominion Univ. Research Foundation)

N74-10499

CSCL 20E G3/16

Unclas 15760

INVESTIGATION OF LASER HOLOGRAPHIC INTERFEROMETRIC TECHNIQUES FOR STRUCTURE INSPECTION

A FINAL TECHNICAL REPORT

By
William P. Chu
Research Associate in Chemistry
Old Dominion University

Prepared for the
NATIONAL AERONAUTICS AND SPACE ADMINISTRATION
Langley Research Center
Hampton, Virginia 23665

Under
Research Grant NGR 47-003-069

Submitted by the
Old Dominion University Research Foundation
P.O. Box 6173
Norfolk, Virginia 23508

October 1973

INVESTIGATION OF LASER HOLOGRAPHIC INTERFEROMETRIC TECHNIQUES FOR STRUCTURE INSPECTION

By

William P. Chu[1]

SUMMARY

The objective of this research effort was to investigate the application of laser holographic interferometric techniques for nondestructive inpection of material structures commonly used in aerospace works. Two types of structures, composite plate and solid fuel rocket engine motor casing, have been investigated in this report.

In conducting the experiments, both cw HeNe gas lasers and Q-switched ruby lasers have been used as light sources for holographic recording setups. Different stressing schemes were investigated as to their effectiveness in generating maximum deformation at regions of structural weakness such as flaws and disbonds. Experimental results on stressing schemes such as thermal stressing, pressurized stressing, transducer excitation, and mechanical impact are presented and evaluated.

INTRODUCTION

One of the problems in the evaluation of engineering material structures is the identification of all internal defects. Defects in the structure can severely limit the performance of the structure component and, in the extreme case, can cause performance failure.

Defects such as internal disbonds have been known to occur frequently in adhesive bond structures, particularly in the high strength filamentary materials

---

[1] Research Associate in Chemistry, Old Dominion University, Norfolk, Virginia 23508

known as composites. The composite is a shell structure formed by aligning high strength fibers in an epoxy or metal and bonding or fusing this material to a substrate. Due to current fabrication processes, numerous bond defects occur either between individual fiber plies or between plies and metal substrate. Since the composite structure is highly inhomogeneous, detection of disbonds is extremely difficult.

Performance of solid fuel rocket engine motors is also vulnerable to internal structure defects. Defects such as propellant cracks, propellant voids, or propellant/case/insulator separation can naturally occur after casting of the propellant grain. If left undetected, the defects could propagate during motor ignition and cause performance failure.

Current nondestructive testing techniques for detection of internal defects in material structures generally involve either radiography, thermography, ultrasonic testing, or the like. These techniques have been somewhat successful, but are not sufficiently sensitive to provide full assurance that all defects can be detected. Moreover, data accuracy concerning the size and location of the various defects is too small by orders of magnitude.

Laser holographic interferometry has recently been introduced as a potentially promising technique for nondestructive testing of material structures [1-4]. The test sample will be placed under stress, and the stress pattern will be recorded holographically. Subsurface defects in the test sample will introduce localized perturbations on the overall stress pattern and can be identified. Since the residual stress distribution around the defect has to be significantly displaced on the sample surface in order to be observed, the most important problem in holographic nondestructive testing would be to evaluate the different stressing schemes for their effectiveness in generating detectable surface stress anomalies.

In this report, we will present some experimental evaluation of laser holographic nondestructive testing technique using various stressing schemes. Two different types of sample will be investigated. One is the composite plate structure, and the other is the solid fuel rocket engine motor casing. The stressing schemes being evaluated will be thermal stressing, pressure stressing, transducer excitation, and force impact excitation. Some theoretical calculations will be performed to correlate experimental data with theoretical predictions.

THEORY OF HOLOGRAPHIC NONDESTRUCTIVE TESTING

Holography is a lensless photographic process in which the complex wavefield associated with an irregular shaped object can be recorded and reproduced [5]. Let $A(x,y)$ denote the reflected complex wave of the object when illuminated by a coherent light source. By interfering this complex wave with a separated coherent plane wave $U(x,y)$, and recording this resulting intensity distribution $I(x,y)$ with a photographic recording medium, we obtain a hologram of the object. Assuming the response of the recording medium is linear with exposure, then the amplitude transmission of the dveloped film will be given by $T(x,y)$ as

$$\begin{aligned} T(x,y) &= T_0 + \beta I(x,y) \\ &= T_0 + \beta(A^2 + U^2 + A^*U + AU^*) \end{aligned} \tag{1}$$

where T_0 is the bias transmission, and β is a constant associated with the recording medium. If this hologram is illuminated with the original plane wave $U(x,y)$, the transmitted wave can be expressed as

$$UT = UT_0 + \beta(U\,U^2 + U\,A^2 + U^2A + U^2A^*) \tag{2}$$

Note that one of the components of the diffracted wave is identical to the object wave originally recorded, aside from a multiplicative constant. Thus we can reconstruct the original object wave from the hologram provided the different components of the diffracted wave in equation (2) can be separated. As is well known, the side-band technique [6] has been widely used in spatially separating the desired component.

Since the holographic process can record and reproduce both the amplitude and phase of a complex wavefront, it is well suited for interferometric works particularly in measuring small surface displacements. There are two types of holographic interferometry which are of interest to us: they are double-exposure and time-averaged holographic interferometry. We will discuss them separately below.

In double-exposure holographic interferometry, holograms of an object in its original state and perturbed state are recorded on the same photographic film. If A_1 and A_2 denote respectively the wavefields corresponding to

the two states, then upon reconstruction we can generate a coherent sum of the two waves $A_1 + A_2$, which will mutually interfere. For small object displacement between the two exposures, the two waves A_1 and A_2 will have the same amplitude distribution but a slightly different phase distribution, which can be expressed as $A_1 = O\exp(i\theta_1)$, and $A_2 = O\exp(i\theta_2)$. Consequently, the reconstructed image intensity of the object will be given by

$$I_{image} = |A_1 + A_2|^2 = 2\,O^2 \left\{1 + \cos\,(\theta_1 - \theta_2)\right\} \tag{3}$$

The phase difference $(\theta_1 - \theta_2)$ can be expressed for a point on the surface as

$$\theta_1 - \theta_2 = (2\pi/\lambda)\,\vec{\Delta r} \cdot (\hat{n}_1 + \hat{n}_2) \tag{4}$$

where $\vec{\Delta r}$ is the vector of displacement of the point, $\hat{n}_1$ and $\hat{n}_2$ are unit vectors from the point to the light source and observation point respectively, and λ is the wavelength of light. The reconstructed image will then be covered with series of fringes: a bright fringe is produced whenever $(\theta_1 - \theta_2) = 2n\pi$, and $n = 0, 1, 2, \ldots$ Thus object surface displacement in the order of a wavelength of light can easily be detected with the double-exposure holographic technique.

The time-averaged technique consists of holographically recording an object while it is subjected to cyclic vibratory motion. The exposure time in the recording has to be long compared to the period of the vibration cycle. Upon reconstruction, an ensemble of images corresponding to images at different times within the vibration cycle will be reproduced. This can be expressed as a time average

$$A = (1/T)\int_0^T O\exp(i\,\theta\cos\omega t)\,dt = O\,J_0\,(\theta) \tag{5}$$

where T is the exposure time, ω is the vibrational frequency of the object, J_0 is the zero order Bessel function, and $T >> 1/\omega$. From equation (5), the reconstructed image intensity will be modulated with the fringe function $J_0^2(\theta)$. Since the maximum of $J_0^2(\theta)$ is at $\theta = 0$, regions without surface motion corresponding to nodal lines of the vibrational pattern will show up with the greatest intensity due to constructive interference of the wavefronts. This

technique has been used extensively for vibrational measurement of plate and shell structures.

In applying holographic interferometric technique for the inspection of plate or shell type structures, surface displacement of the sample under stress will be recorded holographically. The resulting reconstruction will exhibit a fringe pattern indicating the whole surface displacement due to the applied stress. If a localized flaw exists, residual stress distribution around the defect will show up as fringe anomalies. These fringe anomalies, when properly interpreted, can give information on the shape, size, and nature of the flaw.

It is obvious from the above discussion that the final problem in holographic nondestructive testing technique is the interpretation of the resulting fringe pattern characterizing the stress distribution. This would require detailed knowledge of the physical properties of the test sample from which structural response to the applied stress can be predicted. Then the response of the defect to the applied stress has to be computed and superimposed on the overall stress distribution. This is a very complicated problem even for a simple structure with a very simple defect. In this study we will not attempt to pursue the rigorous elasticity calculation. A simple model for the different structures and defects will be assumed and approximate results will then be worked out for comparison with experimental results.

HOLOGRAPHIC NONDESTRUCTIVE TESTING ON COMPOSITE TYPE STRUCTURES

1. Introduction

Composite is a new class of material structures which is lighter, stronger, and more reliable than the conventional homogeneous material structures. It is generally a shell structure formed by aligning high strength fibers such as boron and carbon in an epoxy and bonding this material to a substrate. Current fabrication techniques tend to introduce numerous bond defects either between individual fiber plies or between the plies and the substrate. Detection of these disbonds is necessary to insure the reliability of this type of material structure.

In this report, holographic interferometric technique will be used for

identification of disbonds in the composite type structure. Three test samples will be investigated here. Three stressing schemes including pressure stressing, transducer excitation, and impact excitation will be applied to the samples, and the results evaluated.

2. Samples description

Two different types of composite structure have been investigated experimentally. The first type consisted of a boron/epoxy composite bonded to a titanium substrate. A test sample with programed flaws made of 100-micron thick resistance-welded stainless steel bags is used. This sample (hereafter referred to as sample I) consisted of 12 simulated flaws located as shown in Figure 1. The horizontal rows of flaws are positioned in successively deeper plies from the top of the sample to the bottom. The second type of composite structure consisted of two thin layers of dural, one layer 0.025-inch thick and one 0.065-inch thick, bonded together. Two 8"x8" plates having simulated disbonds made of 12 circular mylar inserts were used as test samples. The locations of the disbonds for sample II are shown in Figure 2. Locations of disbonds for sample III are not known.

3. Pressure stressing scheme

Recently, holographic nondestructive testing using the pressure stressing scheme has been applied to the inspection of honeycomb panel structure with good results [7]. In this section, the pressure stressing scheme will be applied to the three composite plates.

An air-tight chamber, in this case a glass bell-jar, with the test sample enclosed is used in these experiments. The holographic setup consisted of a 50 mw HeNe cw laser (Spectra Physics model 125). The laser output beam is split into a reference beam and an object beam by a variable beam splitter. Double-exposure holograms of the composite plate enclosed in the glass bell-jar are then recorded with various pressure differentials. All holograms in these experiments are recorded on Agfa 10E75 photographic plates. Reconstruction of the hologram is done with the reference beam only.

Figures 3 to 5 illustrate the reconstructions of the double-exposure holograms for the three samples under different pressure changes. Comparison

with Figures 1 and 2 indicates that all the disbonds in sample I and sample II can be identified, whereas only three disbonds can be identified on sample III.

Notice that in all the reconstructions shown in Figures 3 to 5, disbonded areas show up as fringe contours, indicating high forward displacements of the disbonded regions as compared with the bonded region. This can be explained with a simple model for the disbonded structure. Assume a circular disbonded layer can be considered as a thin circular plate with clamped edge. Reducing the external pressure in this case will correspond to a uniform pressure applied internally to the clamped plate, resulting in forward deflection. Assuming the plate structure is homogeneous and can be characterized with radius b, thickness t, Young's modulus Y, and Poisson's ratio ν, the normal deflection w under uniform pressure of magnitude P_o is given by [8]

$$w = (3/2)\, P_o(1 - \nu^2)\ (b^2 - r^2)/Yt^3 \qquad (6)$$

where r is measured from the center of the plate. The maximum normal deflection for a pressure change of ΔP which is at the plate center is given by

$$w_{max} = (3/2)\, \Delta P\ (1 - \nu^2)\ b^4/Yt^3 \qquad (7)$$

which indicated that the maximum deflection is proportional to the fourth power of the plate radius, directly proportional to the applied pressure change, and inversely proportional to the third power of the plate thickness.

Comparison of the predictions from the simple model with the experimental results can be seen in Figure 6. Figure 6a is a plot of relative maximum deflection versus pressure change, showing the linear dependence. Figure 6b is a log-log plot of relative maximum deflection of the disbond versus disbond diameter. The experimental results in this case indicated that the deflection is proportional to the third power of the disbond radius, thus a slight modification of the simple model would be needed. Data for Figures 6a and 6b are obtained from sample II. Figure 6c is a log-log plot of relative maximum deflection versus the inverse of plate thickness, showing the power dependence. Data for Figure 6c are obtained from sample I. In view of the simple model used for describing the disbonds, it is interesting how close the predictions and the experimental results agree.

4. Transducer excitation scheme

Time-averaged holographic interferometric techniques have been widely used for vibrational study of shell type structures using transducer excitation. This technique can also be applied to the identification of disbonds in composite structures by exciting each individual disbonded area into resonance, thus permitting the disbonded area to be detected.

Ceramic transducers attached to the substrate side of the three composite plates are driven by an audio frequency generator and amplifier module. The output frequency can be varied from DC to 600 kHz with 50 watts continuous output. Time-averaged holograms of the three samples were taken with exposure times ranging from 1/4 second to several seconds depending on the beam splitter setting.

In order to record the maximum number of disbonds in a single exposure, the transducer should be driven at a frequency which matches the resonance of most of the disbonds, either in the fundamental or higher overtones. To find the optimum frequency would require taking many time-averaged holograms at different frequencies. This would be a very time consuming task. A simple method of finding the optimum frequency by means of a speckle blurring will be described here.

It is well known that the image of a diffuse object illuminated with coherent light is modulated with a speckle pattern. The speckle size is proportional to the F-number of the imaging system. If a portion of the diffuse surface is under cyclic vibration, the speckle will be blurred. This blurring of the speckle pattern can be observed with the unaided eye focused close to the surface of the object.

In determining the optimum excitation frequency for a particular composite plate, the plate is coated with diffuse white paint and illuminated with the laser output. If the plate is observed with the eyes, localized patches of blurred speckles can be seen to show up and disappear as the excitation frequency is varied. The frequency at which the maximum number of disbonds shows up can be defined as the optimum frequency.

The optimum excitation frequencies for samples I to III were determined by the method described above. Time-averaged holograms were then taken, and

the reconstructions are shown in Figure 7.

From Figure 7, it can be seen that small disbonds are generally difficult to excite. This can be understood by considering the equation describing the fundamental resonant frequency of a clamped circular plate [9]

$$f_1 = 0.47\ (t/b^2)\ \sqrt{\frac{Y}{\rho(1-\nu^2)}} \qquad (8)$$

where ρ is the density of the plate. For small disbonds, where b is small, the frequency for fundamental resonance will be high and the amplitude of vibration small. Thus it would require extremely high excitation frequency and power to detect small disbonds. Information concerning the thickness of the disbonded layer can in principle be obtained by measuring the frequencies for the higher overtones. However, natural disbonds generally occur in irregular shapes, thus making the identification of overtone patterns very difficult.

5. Impact excitation scheme

Another stressing scheme that we will be investigating is the forced impact of the test sample [10]. Transverse waves will be generated and propagated in the sample upon force impact. Defects such as disbonds in the sample will create localized disturbances to the propagating transverse waves. These wave disturbances, when recorded holographically, will show up as anomalies in the reconstructed fringe pattern. By inspecting these anomalies, sizes and locations of the various unbonded regions can be determined.

Since the transverse waves generally propagate with a very high velocity in metallic structures, a pulse laser system has to be used to record the instantaneous amplitude of the transverse waves. The experimental setup for the recording of double-exposure holograms of the transverse waves will be discussed here. Output from a Q-switched ruby laser was split into two beams, an object beam and a reference beam. The object beam was used to illuminate the sample. The reflected light from the sample was superimposed on the reference beam and the interference pattern was recorded on a photographic plate.

The ruby laser used was a Pockel's cell switched ruby laser which normally emits a 10 mjoule, 20 nsec pulse. Since the output coherent length of Pockel's

cell switched ruby laser is generally very short, a specially designed resonant reflector has been used in the laser cavity to narrow the output line-width. This resonant reflector is made of two optically flat quartz pieces: one 2-mm and one 5-mm thick, separated by 25-mm air spacing. A 2-mm diameter aperture has also been placed in the laser cavity to select only the TEM_{oo} mode output.

Transverse waves on the test samples were generated by forced impact with a pendulum. The pendulum was made of a 1.59-cm diameter steel ball attached to a string of 1.5 meters in length. The steel ball was released with a magnetic relay system and achieved an impact velocity of approximately 80 cm/sec. The time interval in which the ball and the test sample are in contact is about 100 μsec, and decreases as the mass of the steel is reduced.

The proper synchronization between the firing of the Q-switched ruby laser and the impact events was accomplished as follows: A cw HeNe laser beam is directed horizontally, cutting the path traveled by the pendulum and illuminating a photodiode. As the steel ball is released from the magnet and cuts through the cw laser beam, a signal is generated from the photodiode. This signal is properly delayed and used to trigger the flash-lamp of the ruby laser. Synchronization of the Pockell's cell unit was achieved by electrically connecting the steel ball and the test sample to a battery. Upon contact of the steel ball with the test sample, a voltage pulse is generated. This pulse is fed into a variable delay generator, and the output from the delay generator is used to trigger the firing of the Pockel's cell. Thus the Q-switched ruby laser can be set to lase at any time after the impact.

Double-exposure holograms of the transverse wave amplitude were recorded with the first exposure taken of the test sample before impact, and the second exposure taken at a preset delay time after the impact.

Experimental results from impact excitation of the three samples are shown in Figures 8 to 11. In Figure 8, sample I was clamped at its four corners with aluminum stiffeners placed along the vertical edges. Holograms of the transverse wave amplitudes were taken at successively later times after the impact. The flaw areas show up as fringe anomalies in the interferograms. Large flaws, such as the triangles in this sample, can be traced out with progessively longer delay recordings. Small flaws, such as the squares and the rectangles, show up as individual vibrating patterns. Figure 9 is another sequence of impact events

for sample I with the stiffeners removed. In this sequence, the triangular flaws are clearly visible. However, the small flaws, particularly the rectangles, do not show up clearly.

Similar anomalies in the reconstructed fringe pattern were also observed when sample I was excited by an impact force of reduced magnitude. This was accomplished by using a smaller steel ball for the pendulum and decreasing the impact velocity. The smaller rectangular flaws were somewhat difficult to detect until stiffeners were placed along the vertical edges of the sample. It is believed that the stiffeners have caused increased local deformation due to the reflection of the impact wave at the boundary. This deformation enhancement is particularly helpful in visualizing smaller flaws.

Experimental results on sample II are shown in Figure 10. One sequence of holograms was recorded and reconstructed. Most of the disbonded areas show up as localized changes in wave amplitude which can be distinguished from the overall symmetric fringe pattern. The wave amplitude distributions within the disbonded areas are generally complex due to the many reflections from the closed boundary. Figure 11 shows the reconstruction of a hologram of sample III. Two disbonds show up on the interferogram. An attempt to locate the rest of the disbonds was not successful.

To determine the sensitivity of the impact excitation scheme in identification of disbonds, we have to consider the perturbing effect of a disbond on the propagating transverse wave. Assume the transmission of transverse waves on a thin plate across a boundary is similar to the case of transverse waves propagating through a boundary between two solid media. The amplitude transmittance going from medium 1 to medium 2 in this case is given by [11]

$$T = 2/(1 + Z_2/Z_1) \tag{9}$$

where $Z_1 = v_1\rho_1$ and $Z_2 = v_2\rho_2$ are the characteristic impedances of the two media, v_i the wave velocity, and ρ_i the density. For transverse waves propagating on a thin plate, the wave velocity, which is dispersive, is given by

$$v_i = (2\pi/\lambda)\sqrt{D/t\ \rho_i} \tag{10}$$

where λ is the wavelength of the transverse waves, $D = Yt^3/96(1 - \nu^2)$.

From equation (9), we see that the change in transverse wave amplitude across the boundary between a bonded and unbonded region will have a complex dependence on the thickness of the bonded and unbonded layers, the amplitude of the incident transverse wave, and the parameters characterizing the material.

We can also consider the situation in which the isolated unbonded region can be driven into oscillation at its principal resonance. This would be similar to the case of using a transducer excitation scheme. Under impact excitation, the time history of the impact force can be approximated by a Gaussian function. The frequency spectrum that can be generated will then be the Fourier transform of the impact force time function. Since the transform of a Gaussian is itself a Gaussian, the transverse wave spectrum will be a Gaussian with a frequency spread inversely proportional to the impact force duration. Thus, unbonded areas with fundamental resonant frequencies matched to the impact force spectrum can be excited and easily observed from the interferogram. It should be mentioned that, because the transverse wave is dispersive, a high frequency wave will generally be highly attenuated the further it propagates. Thus, small unbonded regions away from the impact center will be difficult to excite.

6. Discussion on holographic nondestructive testing of composite plates

Several other stressing schemes have also been tested but without success. Thermal stressing was found impractical due to the high thermal conductivity of the metallic surface material. A static point stressing scheme does not generate sufficient displacement at the unbonded region for detection.

The experimental results concerning pressure stressing, transducer excitation, and impact excitation schemes as discussed in sections 3 to 5 can be briefly summarized here. All three stressing schemes are capable of generating sufficient surface displacement at the disbonded region for detection. Data concerning the size, shape, and thickness of the disbonded layer can be obtained by varying the stressing parameters. These would be the pressure differential in the pressure stressing scheme, output frequency in the transducer excitation scheme, and impact strength and duration in the impact excitation scheme. Comparison between experimental results and predictions from a simple theoretical model of the structure was done for the pressure stressing case and close agreements were obtained.

The experimental results indicated that the sensitivities of the three stressing schemes in detection of small disbonds are of the same order of magnitude. It is reasonable to assume that the minimum size disbond which can be detected will depend not on the different stressing schemes, but rather on the thickness of the unbonded layer. A possible parameter that will characterize this dependence will be the size-to-disbonded layer thickness ratio. From the experimental results, the smallest disbonds which can be detected are the quarter-inch diameter circular disbonds. Considering the thickness of the unbonded layer, which is 0.025-inch, the size-to-disbond thickness ratio is about ten.

Choosing which stressing scheme is to be used in a particular situation will depend on the environment and the structure configuration being inspected. Pressure stressing and transducer excitation schemes are generally easier to apply but require extreme rigidity of the experimental setup. A forced impact scheme requires a more complicated setup, but with the stability requirement greatly relaxed, which make it well suited for field use.

HOLOGRAPHIC NONDESTRUCTIVE TESTING ON SOLID FUEL ROCKET ENGINE MOTOR

A. Holographic inspection of a cutout piece from the rocket engine

An 18-cm by 18-cm cutout piece from a solid fuel rocket engine motor was used as a test sample to perform preliminary evaluation of the sensitivity of holographic nondestructive inspection scheme. The sample was made of a 0.07-cm fiberglass outer case, and a 0.13-cm polymer liner bonded to an inert solid-propellant mixture. Double-exposure holograms were taken while the sample was under thermal stressing. Thermal stress was generated by irradiating the sample surface with a 400-watt quartz lamp for about 10 seconds. Double exposures were then taken with a time interval of one minute to allow sufficient cooling of the sample surface. Figure 12 illustrates one of the reconstructions from the double-exposure holograms. Notice that the sample surface is covered with fringes due to thermal stressing. Three regions of fringe anomalies can be seen which are indicated with arrows on the photograph. These three regions of fringe anomalies, when viewed in a real-time holographic setup, are stationary when the overall thermal fringe pattern is changing. This type of fringe anomaly

has generally been interpreted as an indication of the existence of a disbonded region. The fringe anomalies arise because the air gap created by the disbond will become a barrier to heat flow. Thus the unbonded region will generally be hotter and result in larger thermal expansion.

Destructive testing on the sample was performed by cutting the sample along the C arrows as indicated in Figure 12. The results are shown in Figure 13. Disbonds between the case and the liner exist at locations indicated by the fringe anomalies. Moreover, the dimension of the region of fringe anomalies corresponds to the size of the disbond. Thus we have a very sensitive technique for nondestructive inspection of disbond type defects in solid-fuel rocket engine motors.

B. Holographic inspection of the Scout third-stage casing

1. General description

The test sample in this case was a Scout third-stage rocket engine motor casing 90-cm long and 45-cm in diameter. It consisted of a case layer bonded to an insulation made with fiberglass with a total wall thickness of approximately 1 cm. Double-exposure holograms of the test sample were recorded during either pressure stressing or thermal stressing. Pressure stressing of the test sample was accomplished by changing the internal pressure of the casing. The 400-watt quartz lamp was used to irradiate the sample surface in order to generate thermal stress.

2. Analytical considerations

Since the test sample in this case is simply a thin wall circular cylindrical shell, the response of this structure to an applied stress can be found analytically. First let us consider the problem of pressure stressing by assuming the cylindrical shell is made of homogeneous material. The equation governing the radial displacement of the cylindrical surface w under uniform pressure P is given by [12]

$$\frac{d^2}{dx^2} D \frac{d^2}{dx^2} w + \frac{Yt}{2b^2} w = P \qquad (11)$$

where b is the radius of the circular cylinder, $D = Yt^3/96(1 - \nu^2)$, and

x is the distance along the cylinder axis. For a long cylinder with no edge constraint, the applied pressure P produces only a hoop stress with radial displacement given by

$$w = 2 P b^2/Yt \tag{12}$$

Now let us consider thermal stressing of the cylindrical shell. From the symmetry of the structure, a change in temperature will produce radial displacement of the cylindrical surface due to thermal expansion. The magnitude of radial displacement w will be given by the following equation

$$w = \alpha \Delta T b \tag{13}$$

where ΔT is the temperature change, and α is the linear thermal expansion coefficient of the material.

From equations (12) and (13), we can see that both pressure stressing and thermal stressing will produce uniform radial displacement of the cylindrical shell with no edge constraints. For a simply-supported cylindrical shell, regions away from the edges will also have uniform radial displacement. Thus the remaining problem would be to compute the fringe function in a double-exposure holographic interferometer. However, the fringe function is strongly dependent on the geometry of the experimental setup--the positions of the light source and the observation point with respect to the cylindrical shell. Even for a simple geometry with normal illumination and normal viewing, the fringe function is not a simple mathematical expression. A detailed calculation of the fringe function for a particular experimental setup is done in Appendix A, for a cylindrical shell with simply-supported edges and undergoing pressure stressing. Numerical results for the case of $w = 5\lambda$ are then plotted with a desk calculator as shown in Figure 14. The dotted lines in Figure 14 correspond to the dark fringes observable in an interferogram. Notice that only the upper half portion of the cylinder is plotted because of the symmetry of the problem. Experimental result with the pressurized Scout casing under similar setup geometry is shown in Figure 15. Similar fringe behavior can be observed except for fringe anomalies near the center of the casing. We will later discuss in detail the fringe anomalies observed here.

Detection of flaws in a cylindrical shell structure under either pressure

stressing or thermal stressing can be performed by the following method. The fringe pattern for any particular setup geometry can be computed analytically assuming a homogeneous structure. Experimental results from the interferograms can then be used for comparison. Any fringe anomaly will then indicate the possible existence of flaws.

3. Thermal stressing scheme

The Scout casing surface was marked with black strips into six sections denoting A, B, C, D, E, and F sections. Penetrant developer type SKD-NF was sprayed over the surface to increase the reconstructed image brightness. The holographic setup consisted of the beam expander for the object beam and the recording medium situated close together and normal to the center of the cylindrical structure. This setup will generate a near-elliptical fringe pattern due to the uniform radial displacement of the cylinder.

Thermal stressing was applied to the test sample in two different modes of operation. In the first mode of operation, the sample surface will be irradiated uniformly with the quartz lamp for about one minute, and allowed to cool for three minutes. Double-exposure holograms will then be recorded with a time interval of one minute. This mode of operation will minimize the occurrence of transient thermal gradient across the sample surface, and insure thermal equilibrium during each exposure. Reconstructions from these holograms are shown in Figure 16.

The second mode of operation consists of uniformly irradiating the sample with the quartz lamp for 30 sec. Immediately afterward the first exposure will be recorded, with the second exposure recorded 50 sec later. In this mode of operation, transient thermal gradient will exist on the sample surface. Figure 17 shows the reconstructions from these holograms.

Comparison between Figures 16 and 17 shows that significantly more fringe anomalies occur in Figure 17. This is to be expected as localized thermal gradients would occur more frequently during transient cooling period. These thermal gradients are probably generated by the nonuniform heating and cooling processes. Results in Figure 16 show no fringe anomalies that could be considered as disbonds. Real-time holographic interferometry has also been used to observe the fringe pattern during thermal stressing. No localized fringe anomaly has

been observed. These results strongly suggest that no detectable disbond exists on this sample.

4. Pressure stressing scheme

Pressure stressing of the sample was performed by sealing the two ends of the cylinder and either applying compressed air or using a vacuum pump to change the internal pressure. It was found that identical results were obtained from either increasing or decreasing the internal pressure of the test sample. Double-exposure holograms of the test sample were recorded by reducing the internal pressure at different increments. Reconstructions of these holograms are shown in Figures 18 to 20. Extensive fringe anomalies can be seen especially along the center of the sample. Moreover, the fringe anomalies are localized for different pressure changes.

An explanation of the fringe anomalies was found by measuring the sample wall thickness. It was determined that the sample wall thickness varies as much as 15% across the whole cylinder, particularly along the center. Locations of thicker regions generally correspond to regions of fringe anomalies. This type of behavior can be explained by considering equation (12). The hoop stress will produce a radial displacement proportional to the inverse of the shell thickness. Thicker regions will then experience less displacement under the same hoop stress. Since no destructive test was performed on this sample, no exact comparison between theoretical predictions and experimental results can be made.

Aside from fringe anomalies indicating varying sample wall thickness, no other type of fringe anomalies have been observed. Contour type fringe anomalies such as those presented on the composite plates have not been observed here. These results indicate that no disbond can be detected using pressure stressing in this sample, in agreement with results obtained from the thermal stressing scheme.

C. Discussion and Conclusions

Experimental works on a cutout piece from a solid fuel rocket engine motor indicated that disbonds between the case and insulation as small as 1 cm can be detected by holographic interferometric technique using the thermal stressing scheme.

The thickness of the outer layer in this case is 0.7 mm, indicating a size-to-thickness ratio of about 15 for optimum detection.

Experimental results using the Scout third-stage casing as test sample show no observable disbond under both thermal and pressure stressing. A transducer excitation scheme has been attempted but was unsuccessful due to the large power output required to drive the whole structure of the sample. The thickness of the outer layer is close to 1/2 cm in this sample. Using the size-to-thickness ratio as a criterion, disbonds of a size less than 5 cm will de difficult to detect. Fringe anomalies in the pressure stressing case were found to be due to varying wall thickness of the sample. This would indicate a very powerful method of inspecting wall thickness uniformity in cylindrical shell structures.

CONCLUSIONS AND RECOMMENDATIONS

Holographic nondestructive testing of shell-type structures has been investigated using different stressing schemes to excite the samples. For composite plate structures, pressure stressing, transducer excitation, and impact excitation schemes are found to be capable of producing sufficient deformation at the unbonded region for detection. The dimension of the smallest size disbond detectable was found to be about ten times the thickness of the unbonded layer. For inspection of solid fuel rocket engine motors, good results were obtained from a cutout piece under thermal stressing. Experimental results with the Scout third-stage casing using thermal and pressure stressing schemes showed no anomaly due to unbonded type defects. Assuming that the minimum size disbond which can be detected is about ten times its thickness, then no disbond larger than 5 cm exists on this sample.

Some future area of interest is the application of holographic inspection technique for the determination of bond quality, not just the size, shape, and location of disbond. This would require considerably more study on the physical properties of the bonded type structures and their responses to different applied stress.

REFERENCES

1. Friesem, A.A., and Vest, C.M.: Appl. Opt., 8, 1253 (1969).
2. Wiswall, C.E., and Maxwell, K.J.: Appl. Opt., 9, 1724 (1970).
3. Erf, R.K., Aas, H.G., and Waters, J.P.: J. Acoust. Soc. Amer., 47, 968 (1970).
4. Waters, J.P.: Appl. Opt., 10, 2364 (1971).
5. Smith, H.M.: Principles of Holography. Wiley-Interscience, New York, 1969.
6. Leith, E.N., and Upatniek, J.: J. Opt. Soc. Amer., 52, 1123 (1962).
7. Waters, J.P.: In Proceedings of the conference on Engineering Applications of Holography, 1972.
8. Timoshenko, S., and Woinowsky-Krieger, S.: Theory of Plates and Shells. McGraw-Hill, New York, 2nd. ed., 1959, p. 56.
9. Kinsler, L.E., and Frey, A.R.: Fundamentals of Acoustics. John Wiley & Sons Inc., New York, 1950, p. 114.
10. Chu, W.P., Robinson, D.M., and Goad, J.H.: Appl. Opt., 11, 1644 (1972).
11. Kolsky, H.: Stress Waves in Solids. Dover, New York, 1963, p. 60.
12. Same as Ref. 8, p. 468.

APPENDIX A

CALCULATION OF THE FRINGE FUNCTION FOR A SIMPLY-SUPPORTED CYLINDER UNDER UNIFORM INTERNAL PRESSURE CHANGE

The equation governing the radial deformation of a thin wall cylinder of radius b is given by equation (11).

$$\frac{d^2}{dx^2} \; D \frac{d^2}{dx^2} \; w \; + \; \frac{Yt}{2b^2} w \; = \; P \tag{11}$$

For a long cylinder with one end simply supported at $x = 0$, the solution to the above equation will then be given by

$$w(x) \; = \; (2Pb^2/Yt) \; \; (1 - e^{-\beta x} \cos \beta x) \tag{A1}$$

where $\beta^4 = Yt/2Db^2$.

A particular experimental setup as shown in Figure 21 was used to calculate the fringe function recorded in a holographic reconstruction. The observation point A is at the origin of the coordinate system, with S the point of illumination, P_o being a point on the cylinder axis, and P_1 being a point on the surface of the cylinder. The coordinates of all these points can be written as

$$\begin{aligned} A &= (0, 0, 0) \\ S &= (a, 0, 0) \\ P_o &= (x, x \cot \Theta + b, 0) \\ P_1 &= (x + R \sin \psi \cos \Theta, x \cot \Theta + b - R \sin \psi \sin \Theta, R \cos \psi) \end{aligned} \tag{A2}$$

where R is the radius of the cylinder, Θ is the angle of inclination of the cylinder axis to the Y axis, and ψ is the angle measured from the Z axis to the cylinder axis along a plane normal to the cylinder axis. Using the equation describing the phase change as $(2\pi/\lambda) \; \vec{\Delta R} \cdot (\hat{r}_1 + \hat{r}_2)$, we have

$$\vec{r_1} = \overrightarrow{S - P_1}$$

$$\vec{r_2} = \overrightarrow{A - P_1} \qquad \text{(A3)}$$

$$\vec{\Delta R} = |\Delta R| \ (\overrightarrow{P_1 - P_0})/|\overrightarrow{P_1 - P_0}|$$

and $\Delta R(x)$ is given by equation (A1).

In order to plot the fringe function as recorded in the reconstruction with a photograph, we have to plot the fringe function in the following coordinate X and Y,

$$X = dx/[x \sin \theta + (b - R \sin \psi) \cos \theta]$$

$$Y = dR \cos \psi/(b - R \sin \psi)$$

where d is a scaling factor. Figure 14 is a resulting plot for $\theta = 45°$, $b = 38$, $a = 10$, and $R = 10$, performed by a desk calculation.

FIGURE CAPTIONS

1. Composite test sample I showing the locations and dimensions of the programed flaws. For this sample, a = 0.625 cm, b = 1.25 cm, c = 2.5 cm, and d = 6.25 cm.

2. Composite test sample II showing the locations and dimensions of the programed disbonds. For this sample, a = 1/4", b = 1/2", c = 3/4", and d = 1".

3. Reconstructions from the double-exposure holograms of sample I under different pressure changes. (a) Pressure difference of 0.5 psi, and (b) pressure difference of 1.5 psi.

4. Reconstructions from the double-exposure holograms of sample II under different pressure changes, with (a) pressure difference of 0.4 psi, (b) pressure difference of 0.8 psi, and (c) pressure difference of 3.5 psi.

5. Reconstruction from the double-exposure hologram of sample III under pressure difference of 2.0 psi.

6. (a) Plot of maximum deflection versus pressure difference for the disbonds showing the linear relationship. Data were taken from results in Figure 4.
   (b) Log-log plot of maximum deflection versus disbond diameter. Data are taken from results in Figure 4.
   (c) Log-log plot of maximum deflection versus the inverse of disbond thickness. Data are taken from the results in Figure 3 for the square flaws.

7. Reconstructions from time-averaged holograms of (a) sample I excited at 60 kHz, (b) sample II excited at 83 kHz, and (c) sample III excited at 57 kHz.

8. Photographs of the reconstructions taken from the first sequence of holograms of sample I showing the variation of fringe pattern with delay time from impact. For this sequence the sample has stiffeners located along the vertical edges.

9. Second sequence of Figure 8 for sample I. The stiffeners were removed in this sequence.

10. Photographs of the reconstructions taken from a sequence of holograms of sample II under impact excitation showing the variation of fringe pattern with two different delay times.

11. Photograph of the reconstruction taken from sample III under impact excitation at 60 μsec after the impact.

12. Photograph of the reconstruction taken from the hologram of the cutout piece under thermal stressing. Arrows indicate the locations of disbonds. Destructive testing was performed by cutting along the C-axis.

13. Results from the destructive test of the cutout piece showing areas of separation between case and liner. Photographs are taken with 3X magnification with (a) corresponding to arrow 1 in Figure 12, (b) corresponding to arrow 2 in Figure 12, and (c) corresponding to area of good bonding.

14. Computer plot of the fringe function as observed in an interferogram due to internal pressure change for a simply-supported thin wall cylindrical shell structure. The maximum radial displacement is 5λ. Only the upper half portion of the cylindrical surface is plotted here. Numerical data for the setup geometry is given in Appendix A.

15. Experimental result obtained from the Scout third-stage casing used for comparison with Figure 14.

16. Photographs of the reconstructions taken from the holograms of the Scout third-stage motor casing under thermal stressing. Efforts to reduce transient thermal gradient were taken in these experiments. (a) Section B of the casing at the center, (b) section D at the center, and (c) section F at the center.

17. Same as Figure 16 except no effort to reduce transient thermal gradient was undertaken.

18. Photographs of the reconstructions taken from the holograms of the Scout third-stage motor casing under pressure stressing. The internal pressure changes are 0.05, 0.1, 0.5, and 1.0 psi. The B section of the casing is situated at the center of the photographs.

19. Same as Figure 18, with the D section at the center of the photographs.

20. Same as Figure 18, with the F section at the center of the photographs.

21. Geometry of the experimental setup used for computation of the fringe function as shown in Figure 14, and also used for recording of holograms with reconstruction as shown in Figure 15.

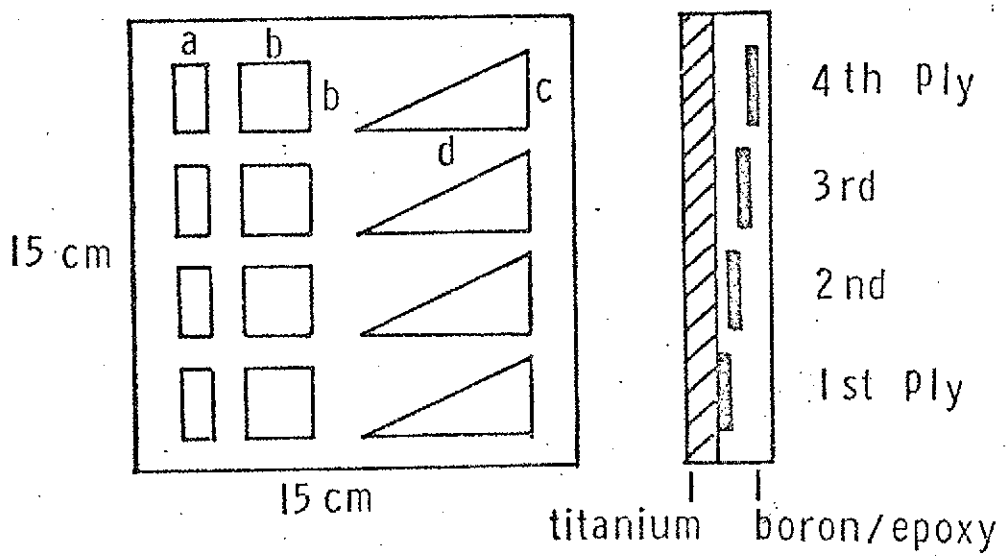

FIGURE 1

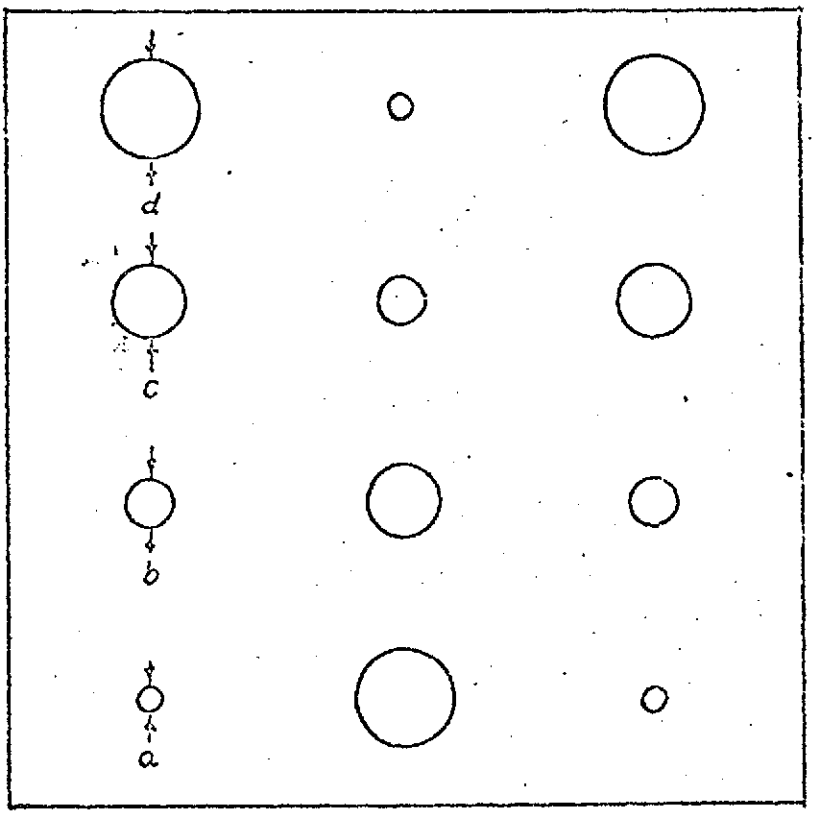

FIGURE 2

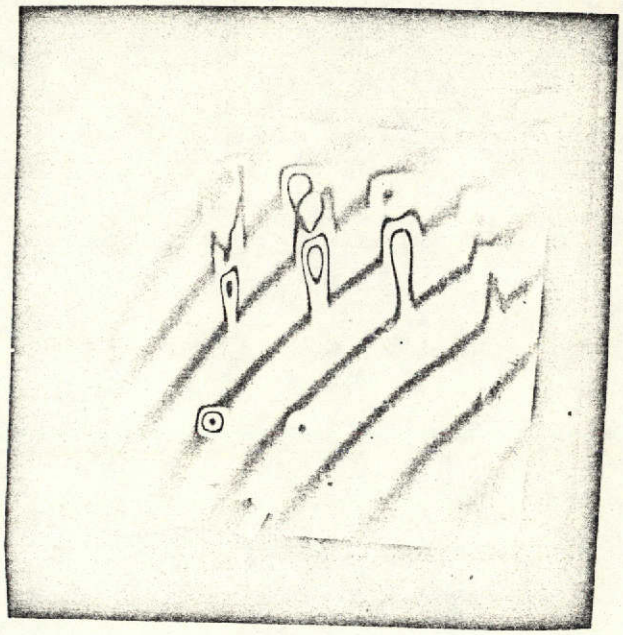

(a)

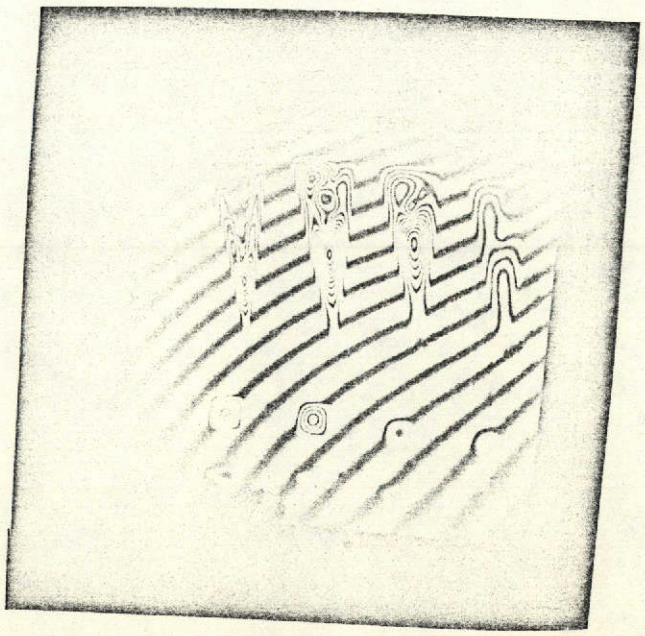

(b)

FIGURE 3

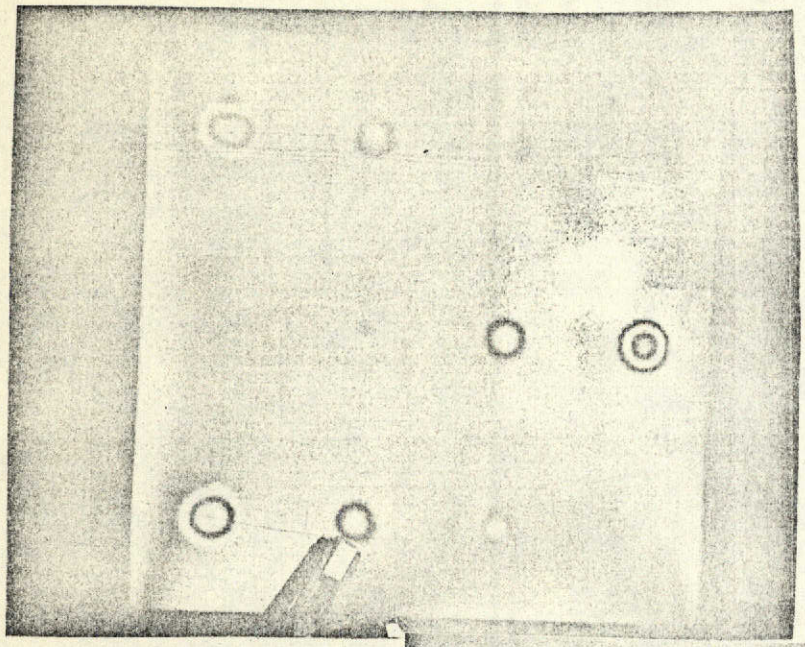

(a)

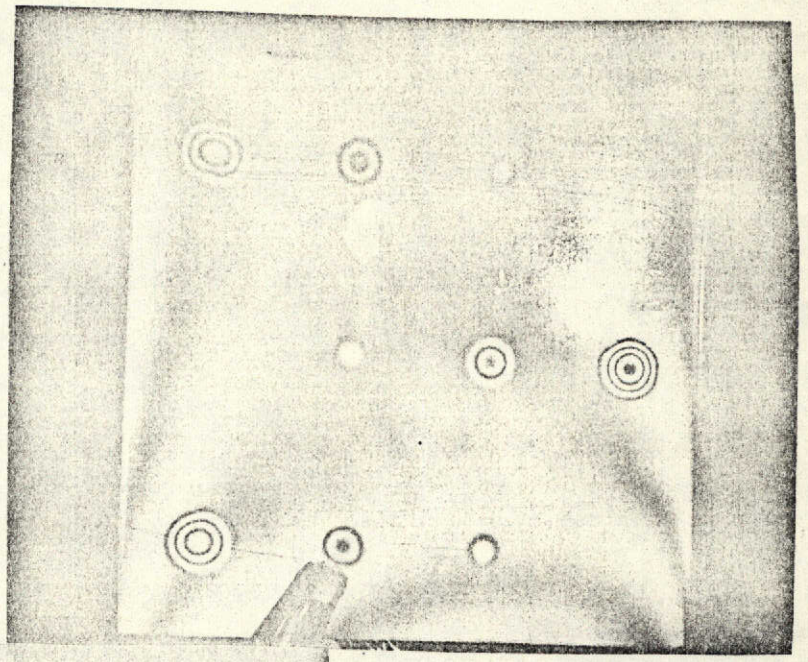

(b)

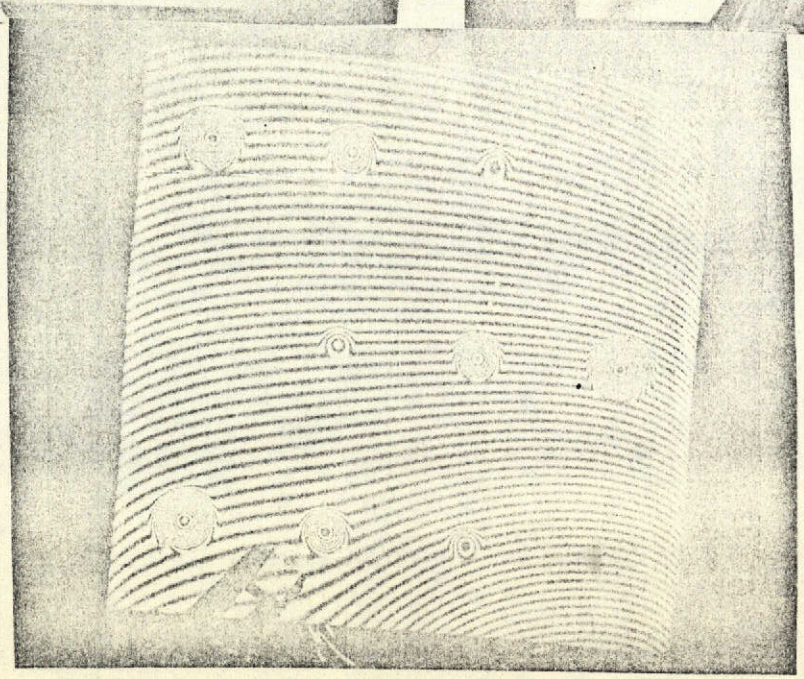

(c)

FIGURE 4

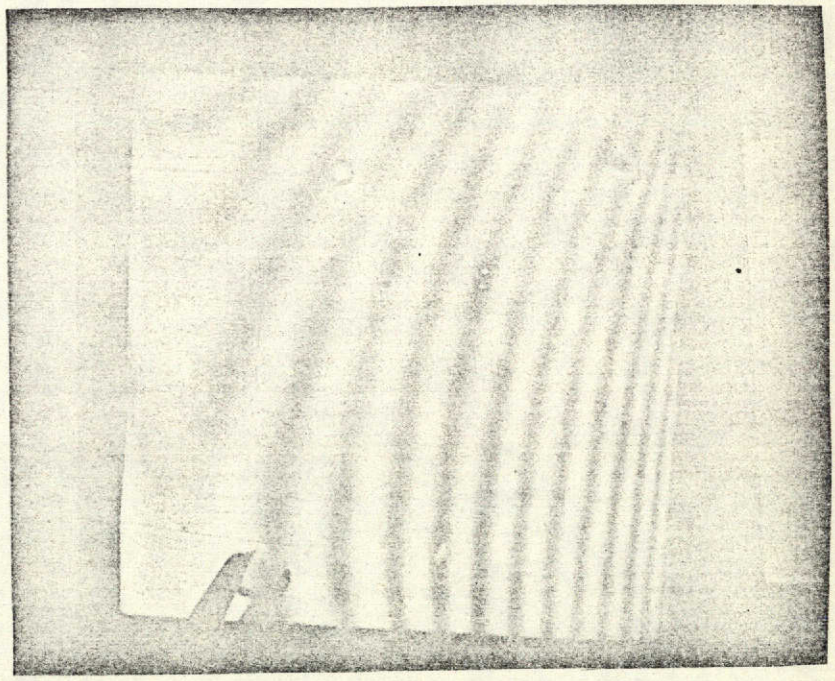

FIGURE 5

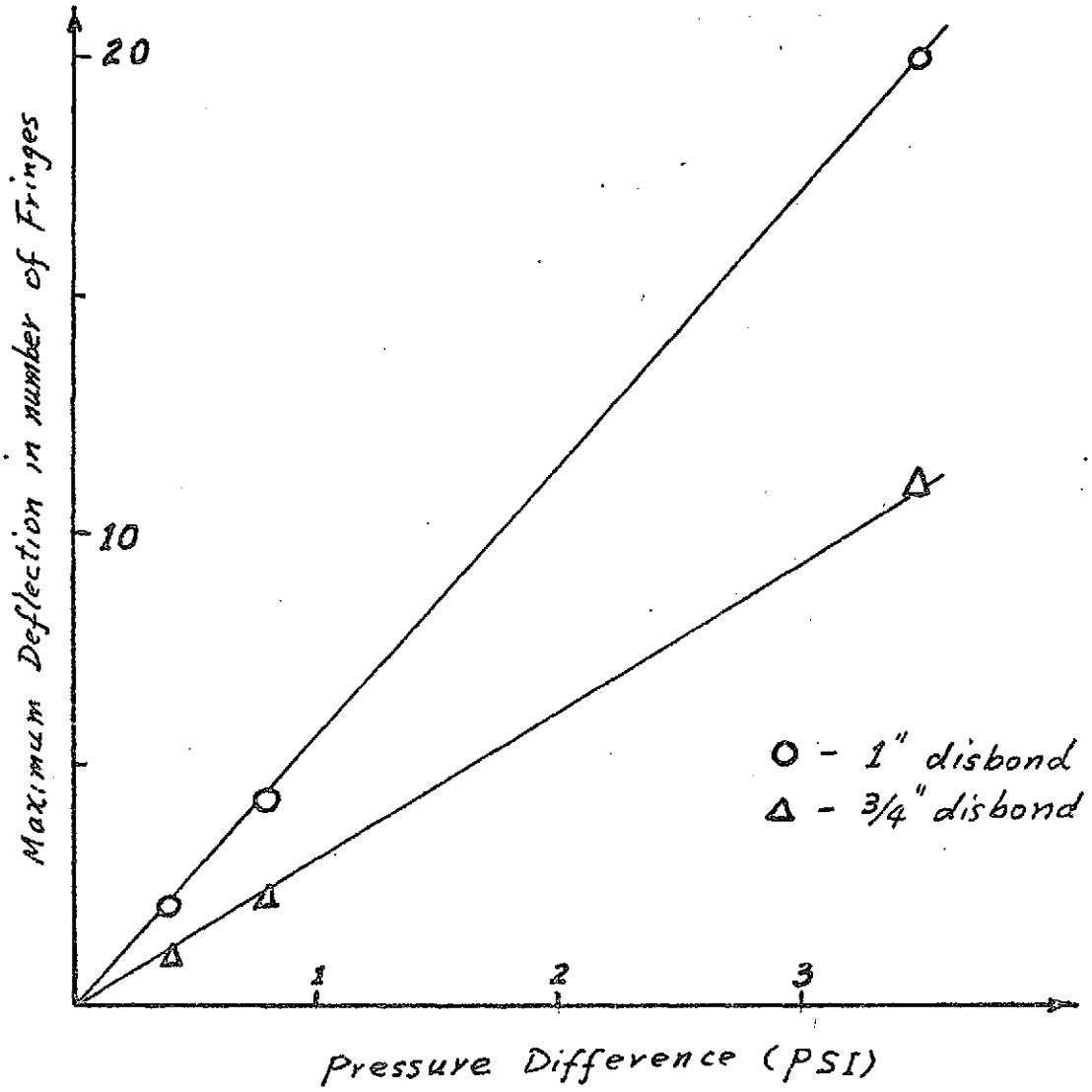
20
10
Maximum Deflection in number of Fringes
1
2
3
Pressure Difference (PSI)
○ - 1" disbond
△ - 3/4" disbond

FIGURE 6 (a)

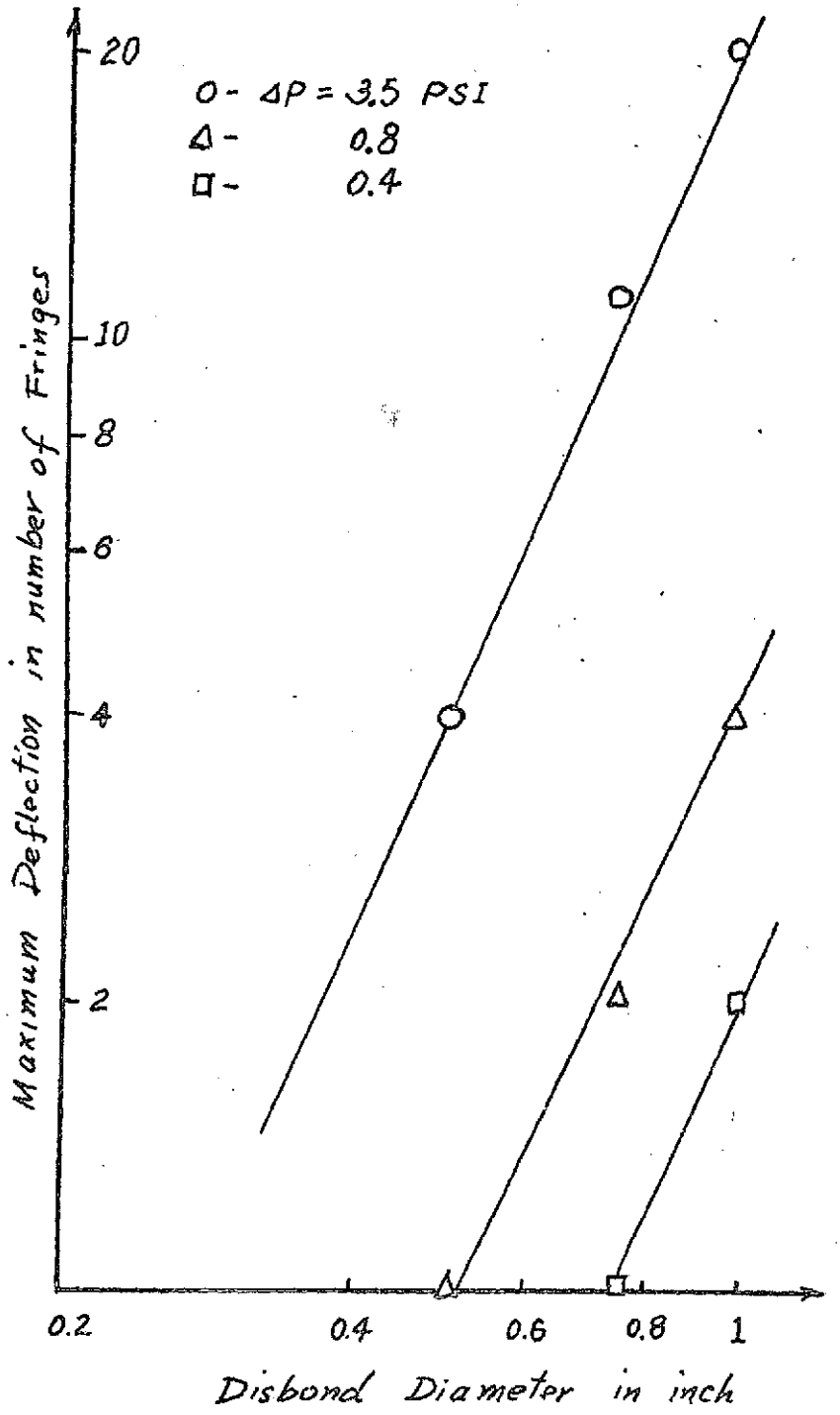
20
10
8
6
4
2
O - ΔP = 3.5 PSI
Δ - 0.8
□ - 0.4
Maximum Deflection in number of Fringes
0.2
0.4
0.6
0.8
1
Disbond Diameter in inch

FIGURE 6(b)

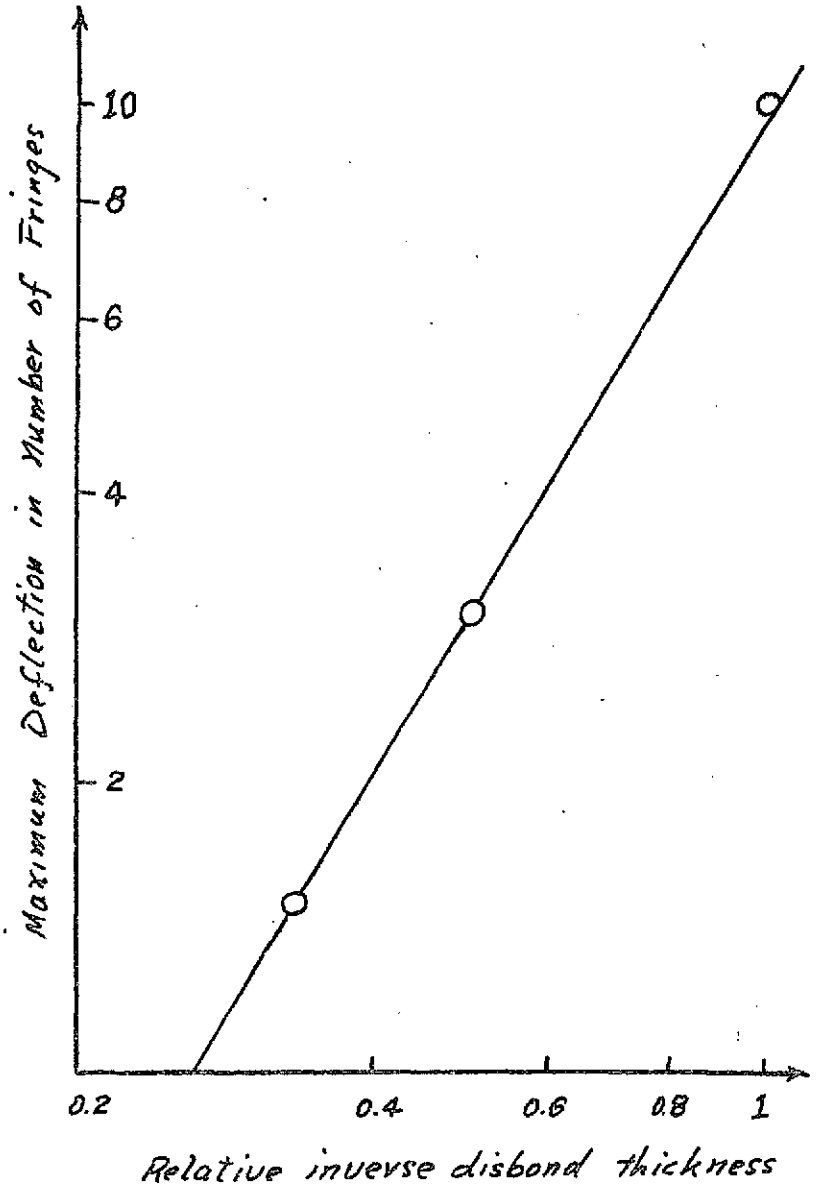
Maximum Deflection in Number of Fringes
10
8
6
4
2
0.2
0.4
0.6
0.8
1
Relative inverse disbond thickness

FIGURE 6(C)

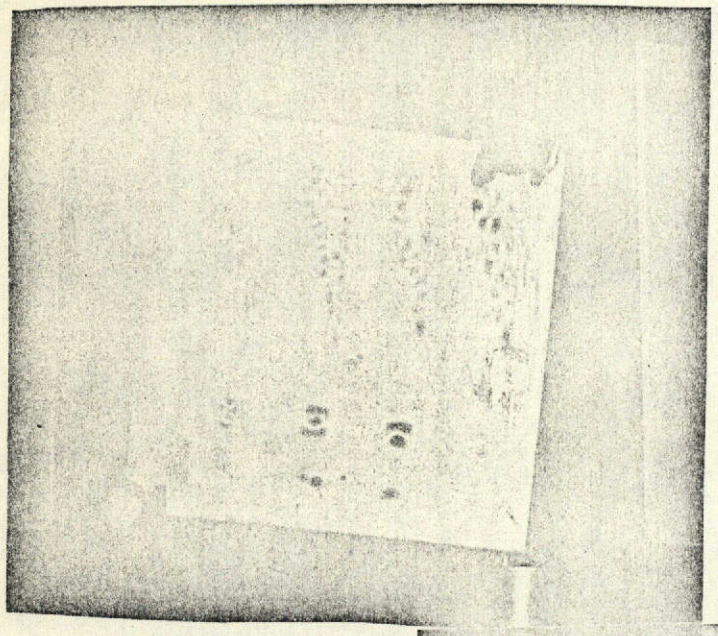

(a)

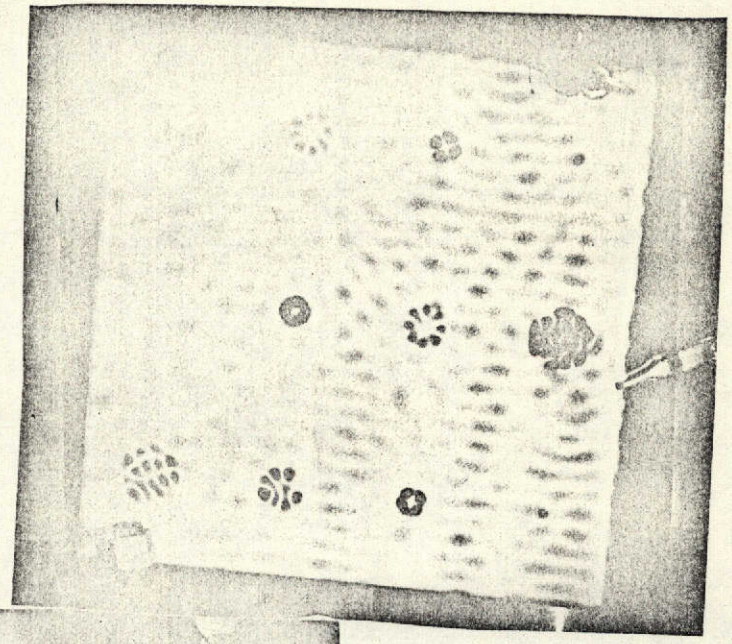

(b)

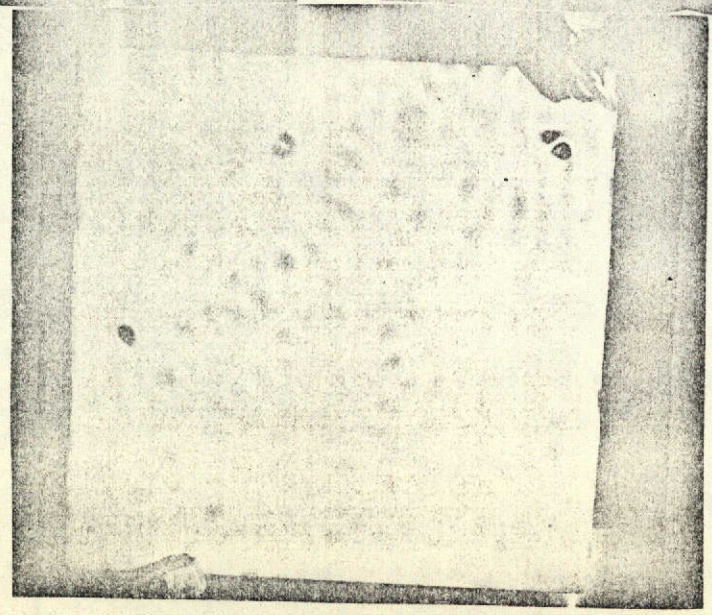

(c)

FIGURE 7

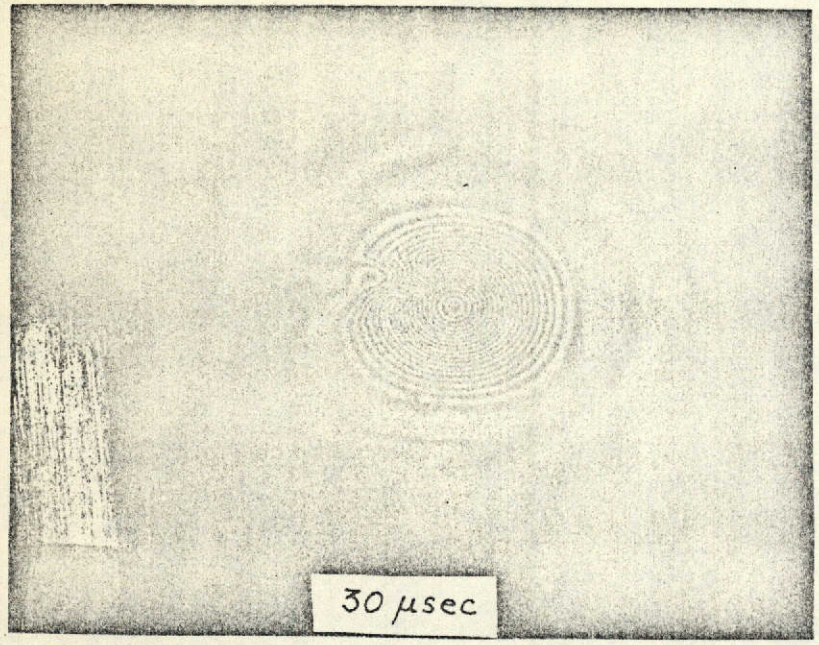

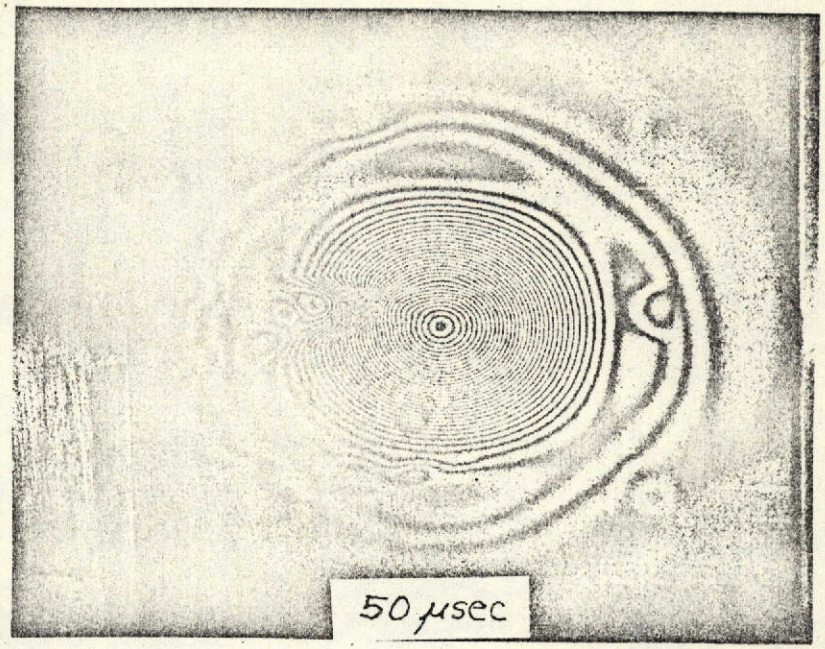

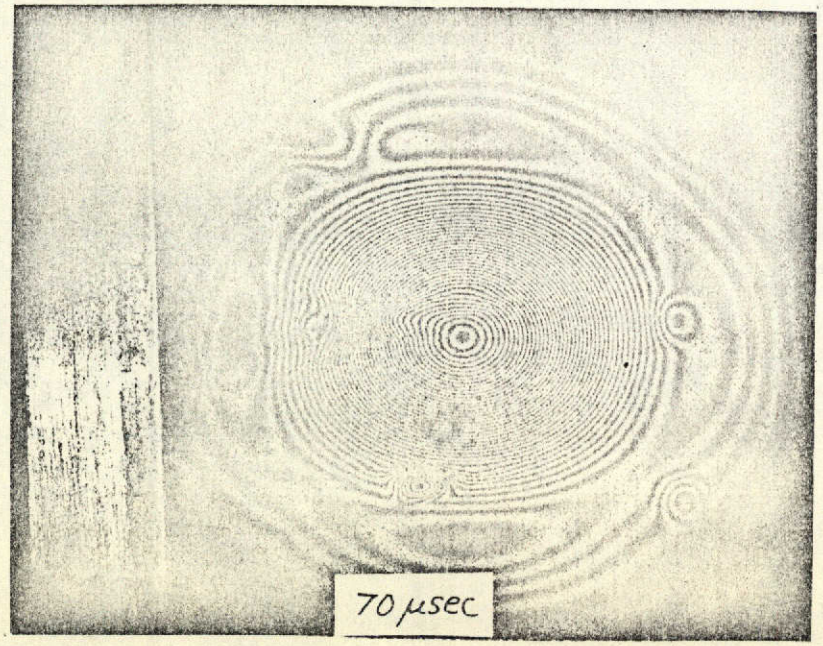

FIGURE 8

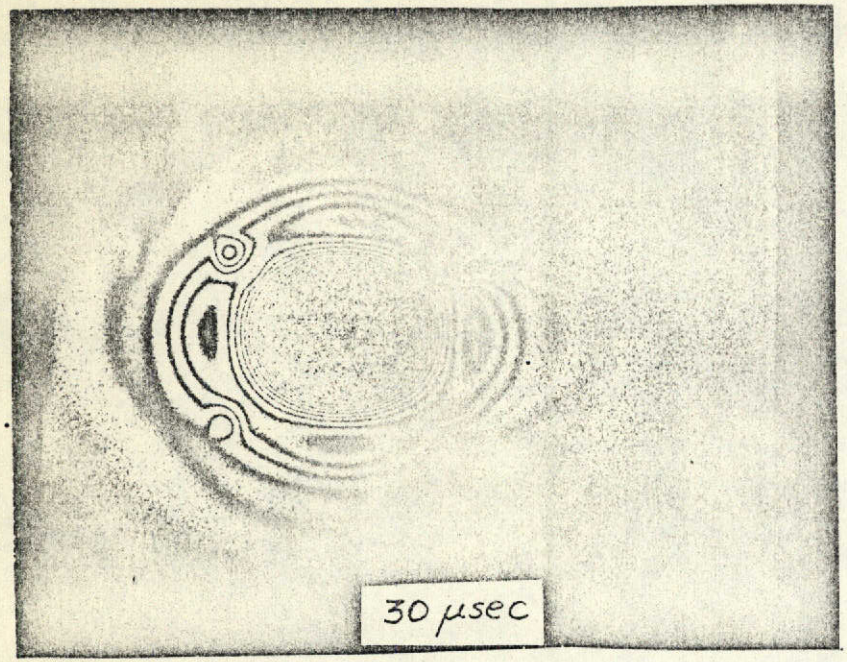

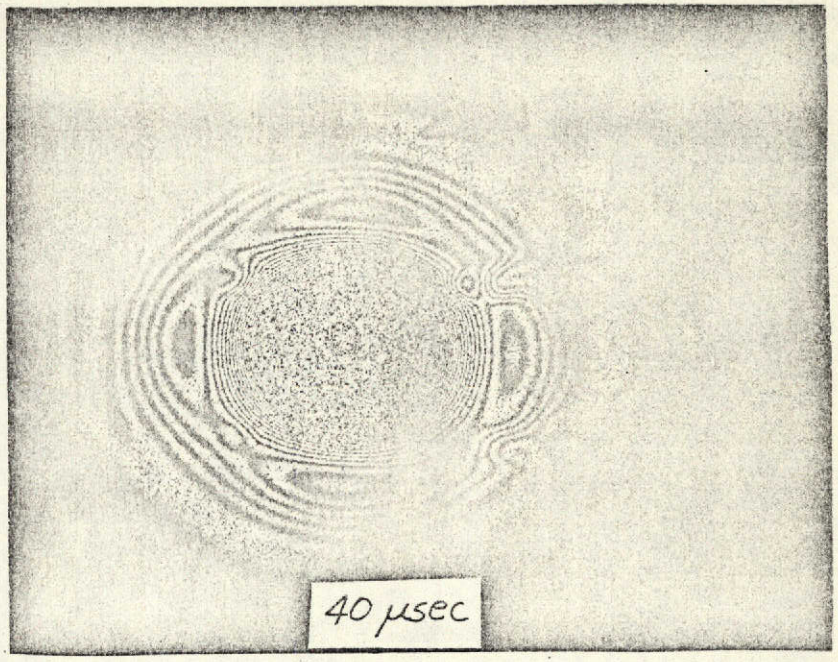

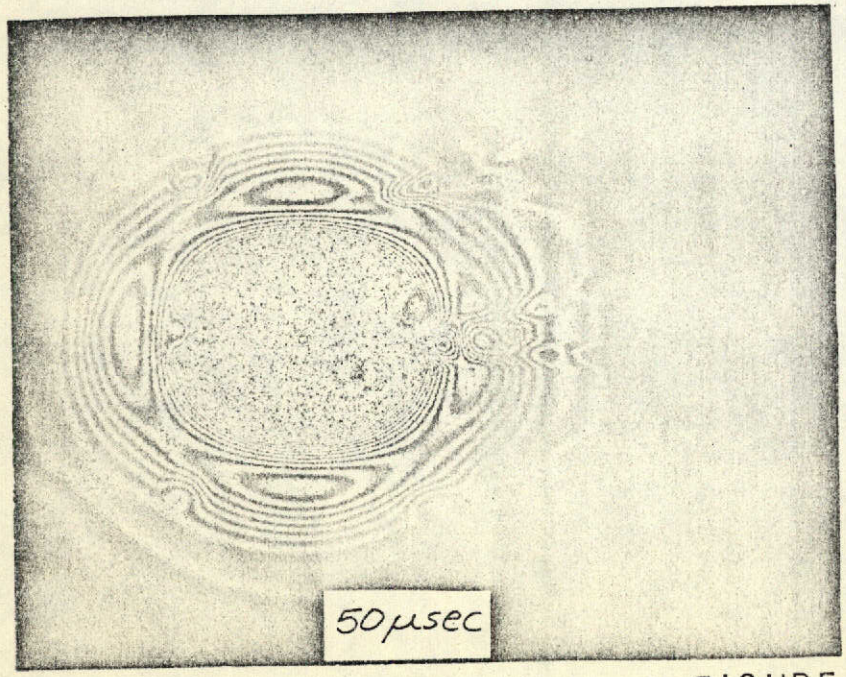

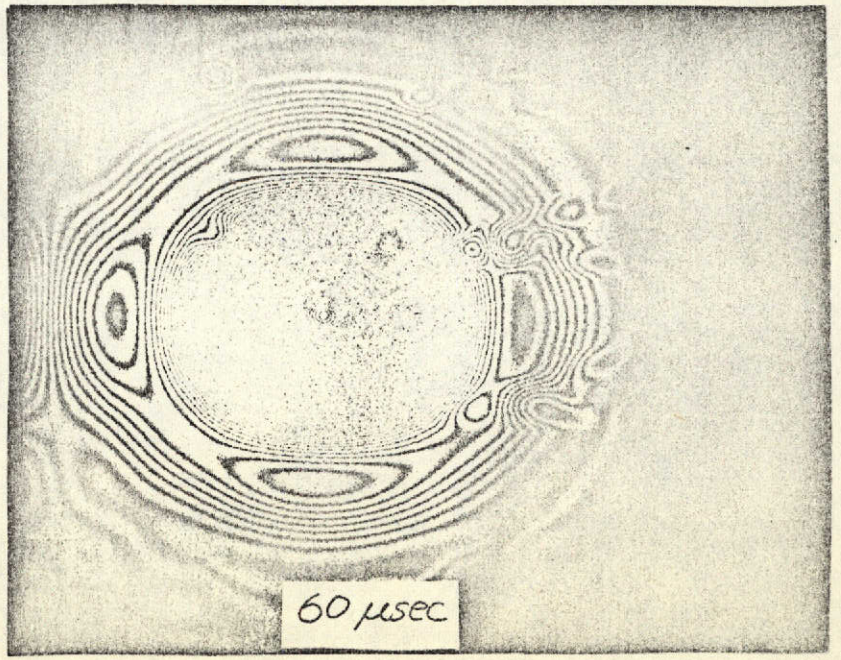

FIGURE 9

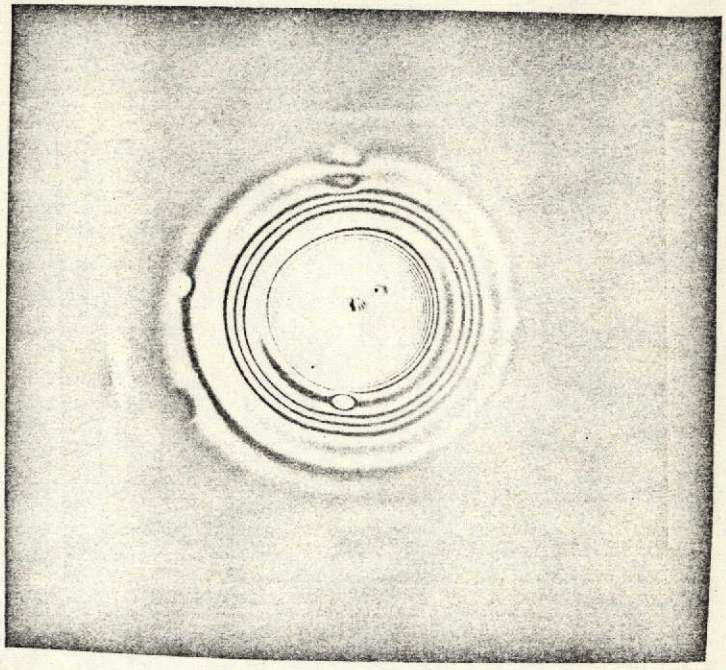

(a) 50 μsec

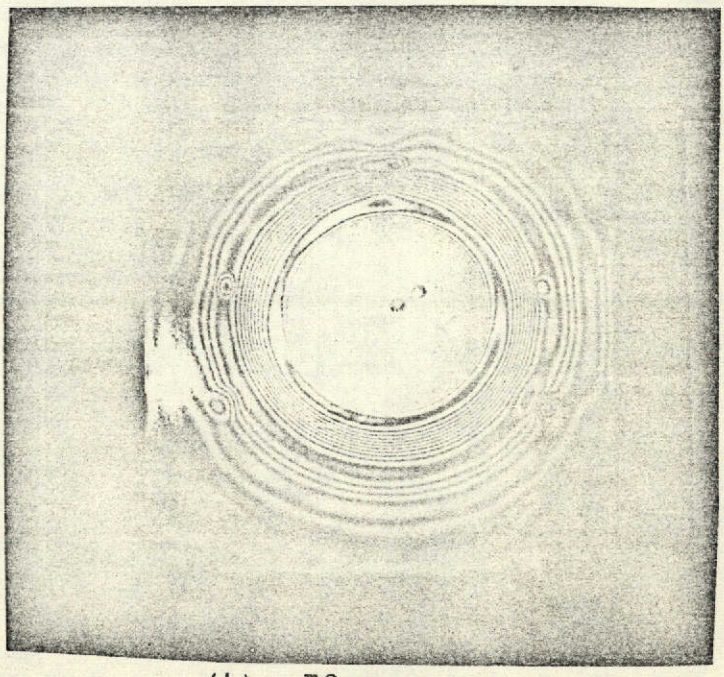

(b) 70 μsec

FIGURE 10

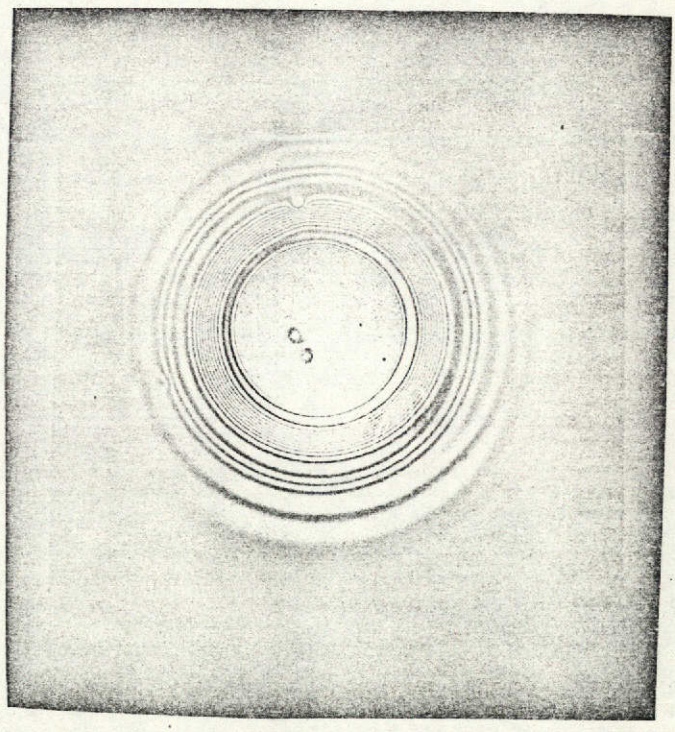

FIGURE 11

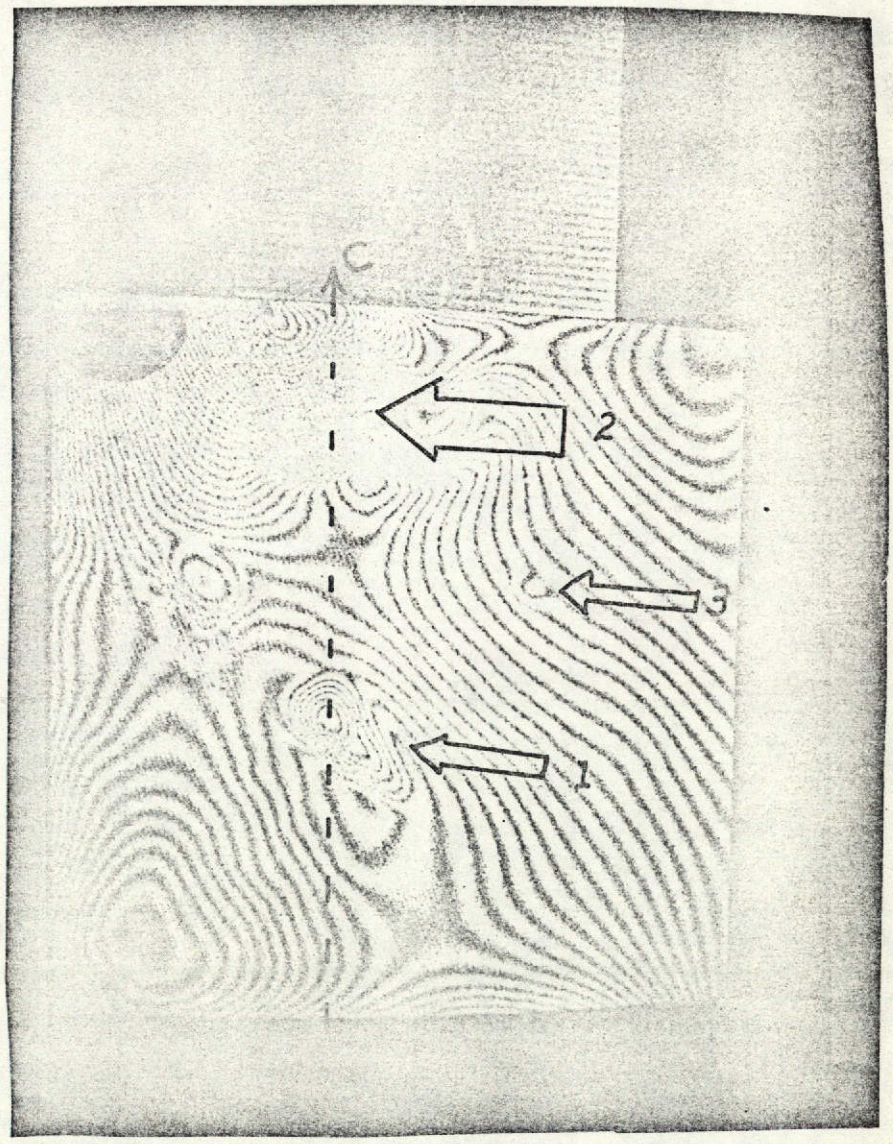

FIGURE 12

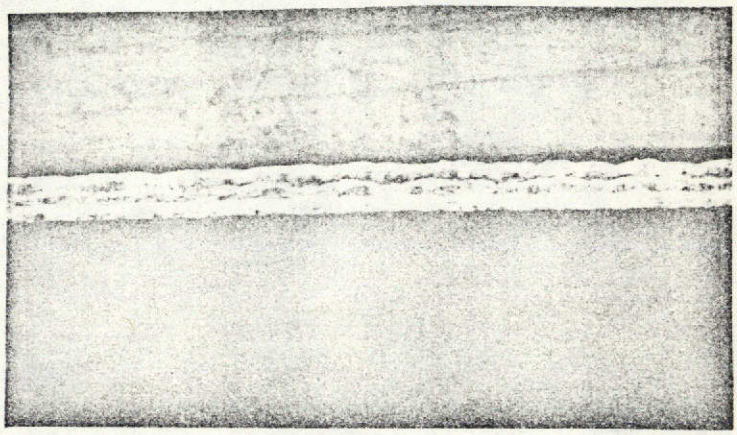

(a)

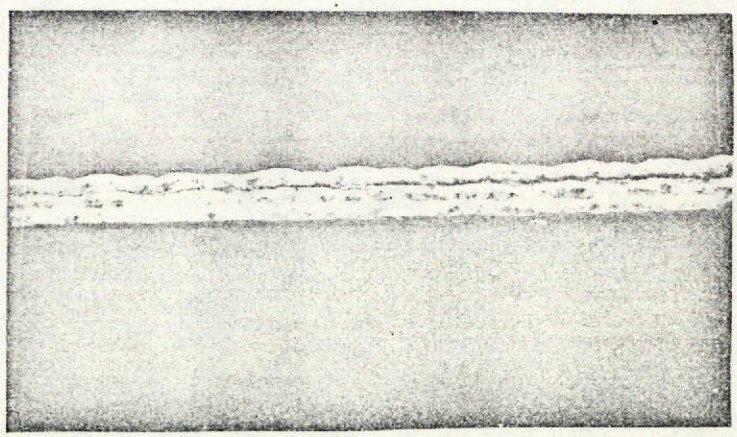

(b)

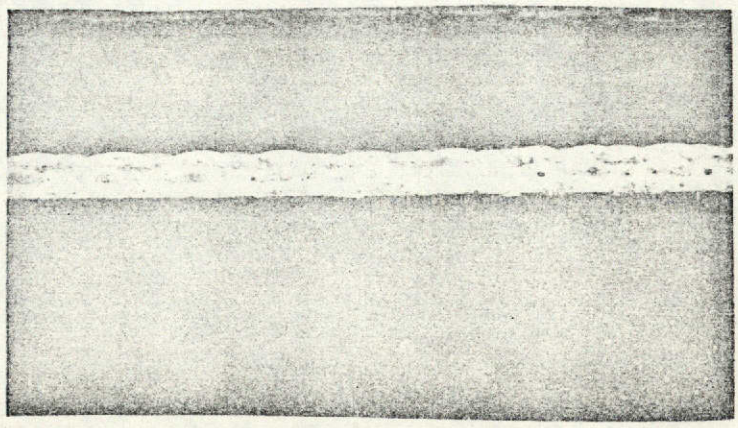

(c)

FIGURE 13

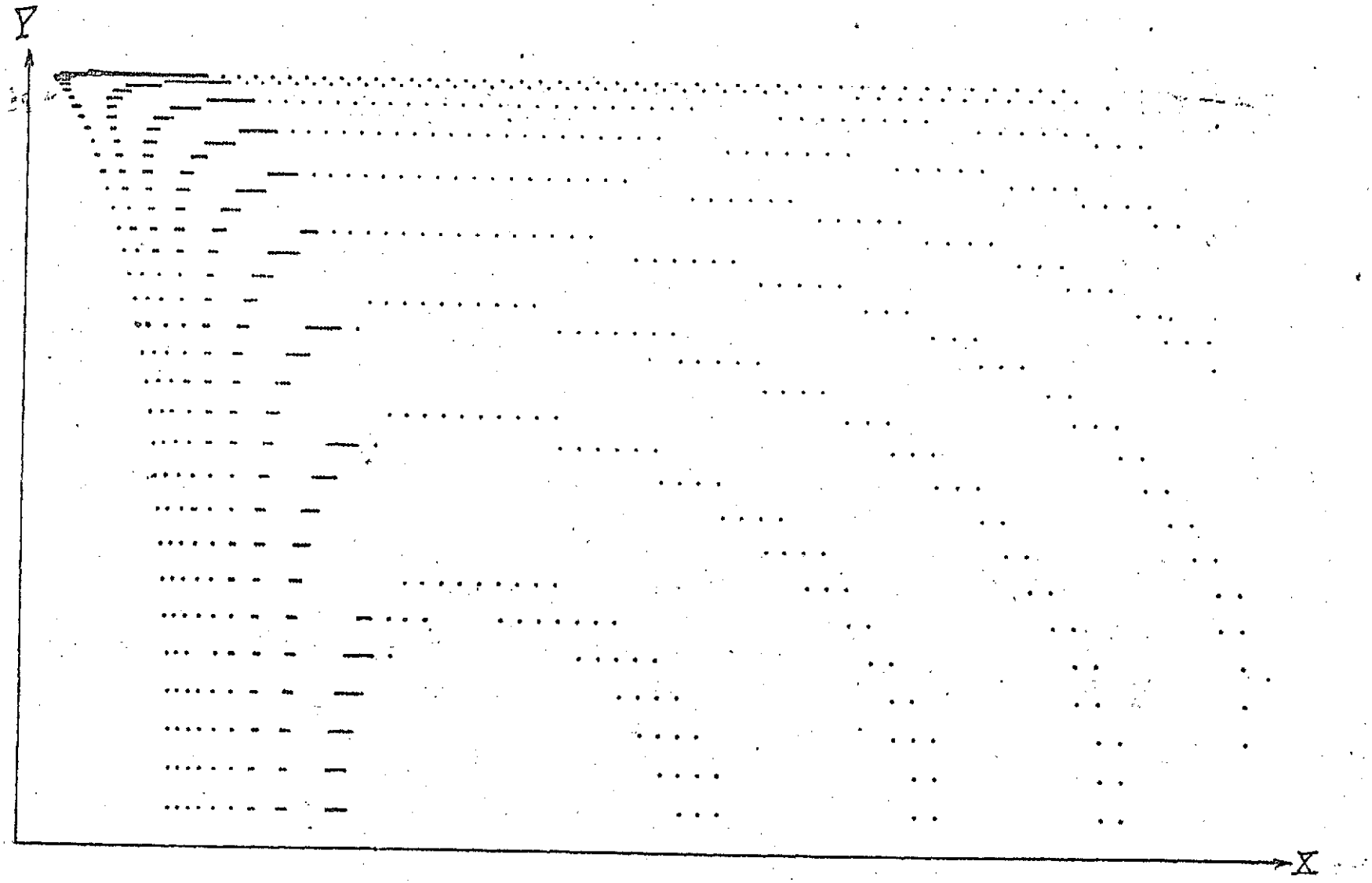

FIGURE 14

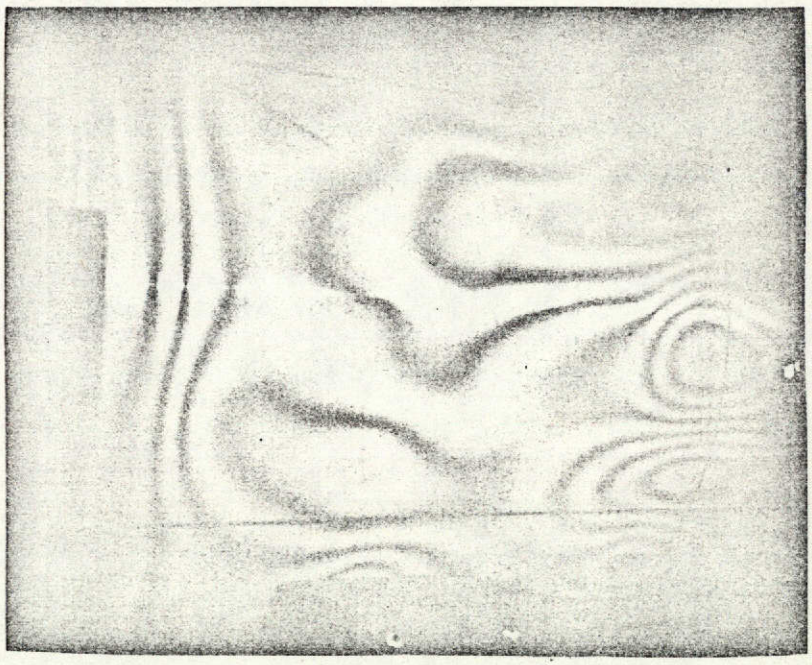

FIGURE 15

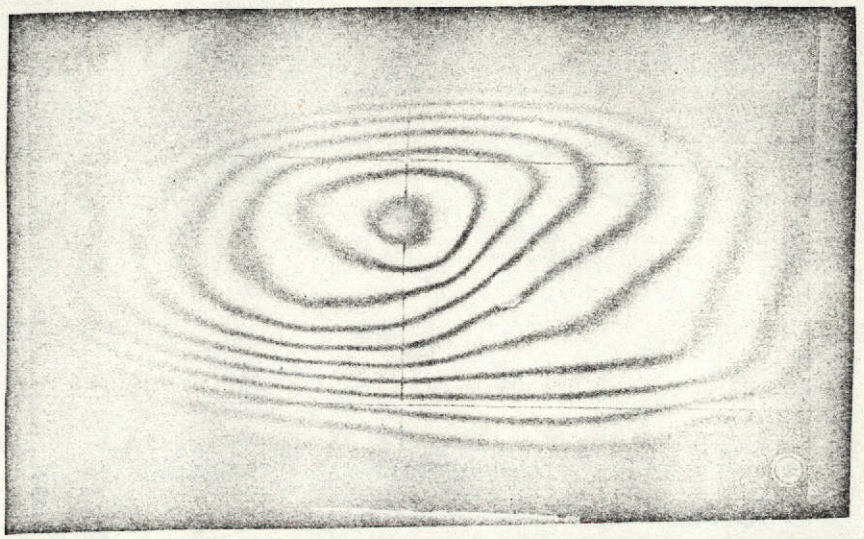

(a)

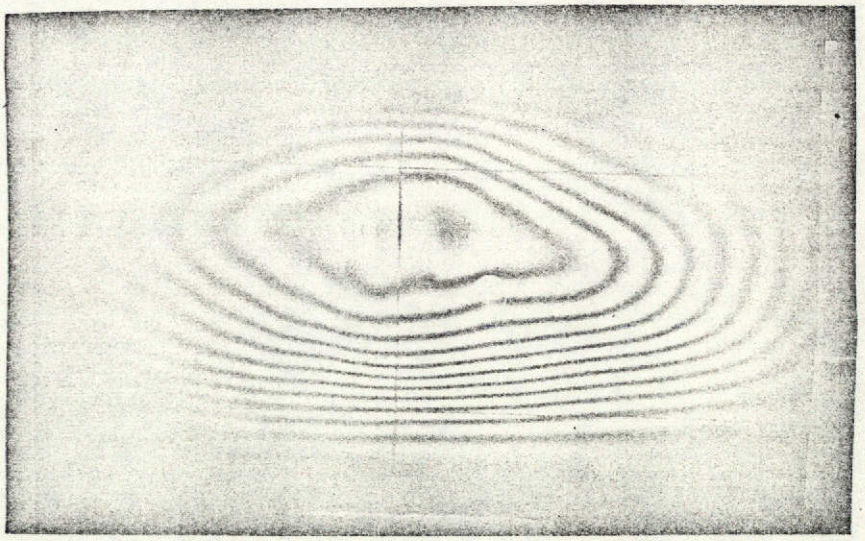

(b)

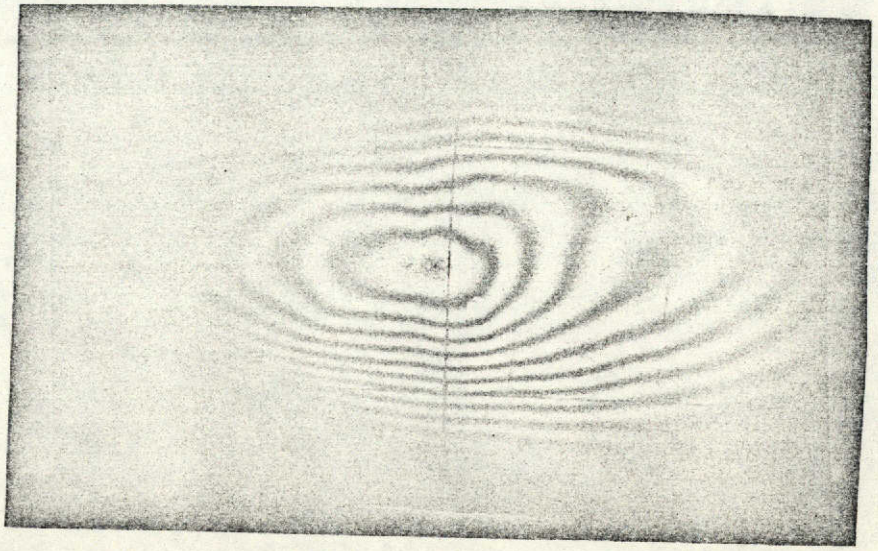

(c)

FIGURE 16

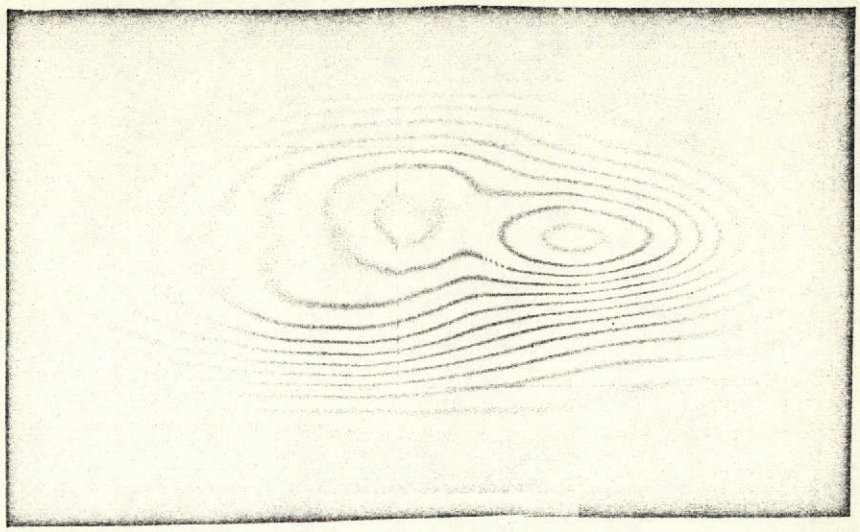

(a)

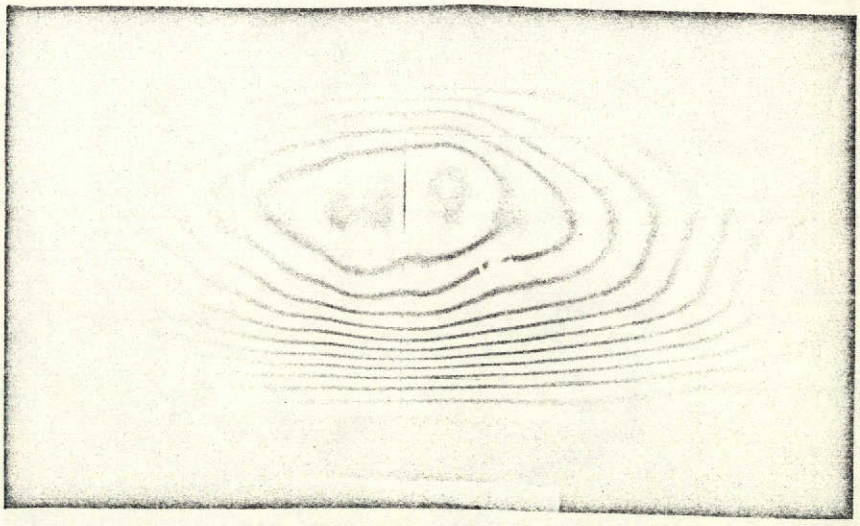

(b)

(c)

FIGURE 17

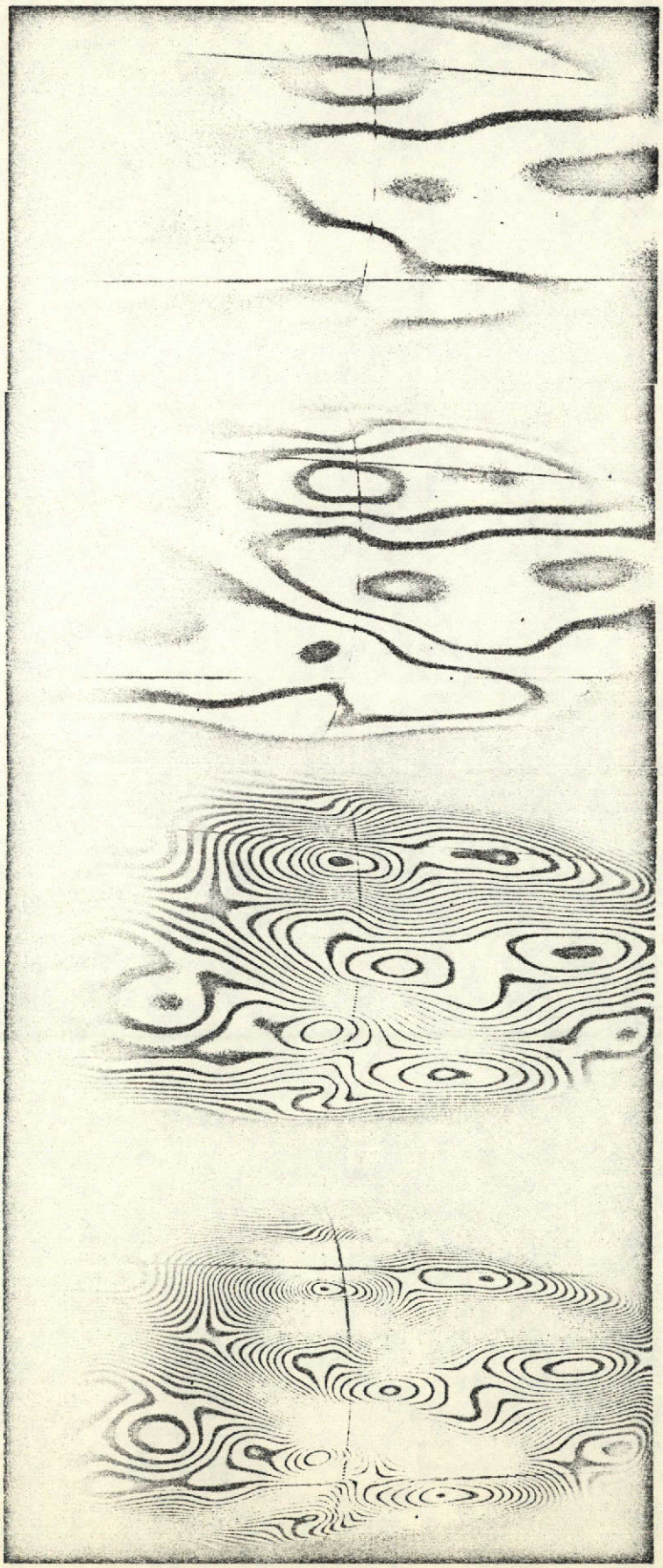

FIGURE

18

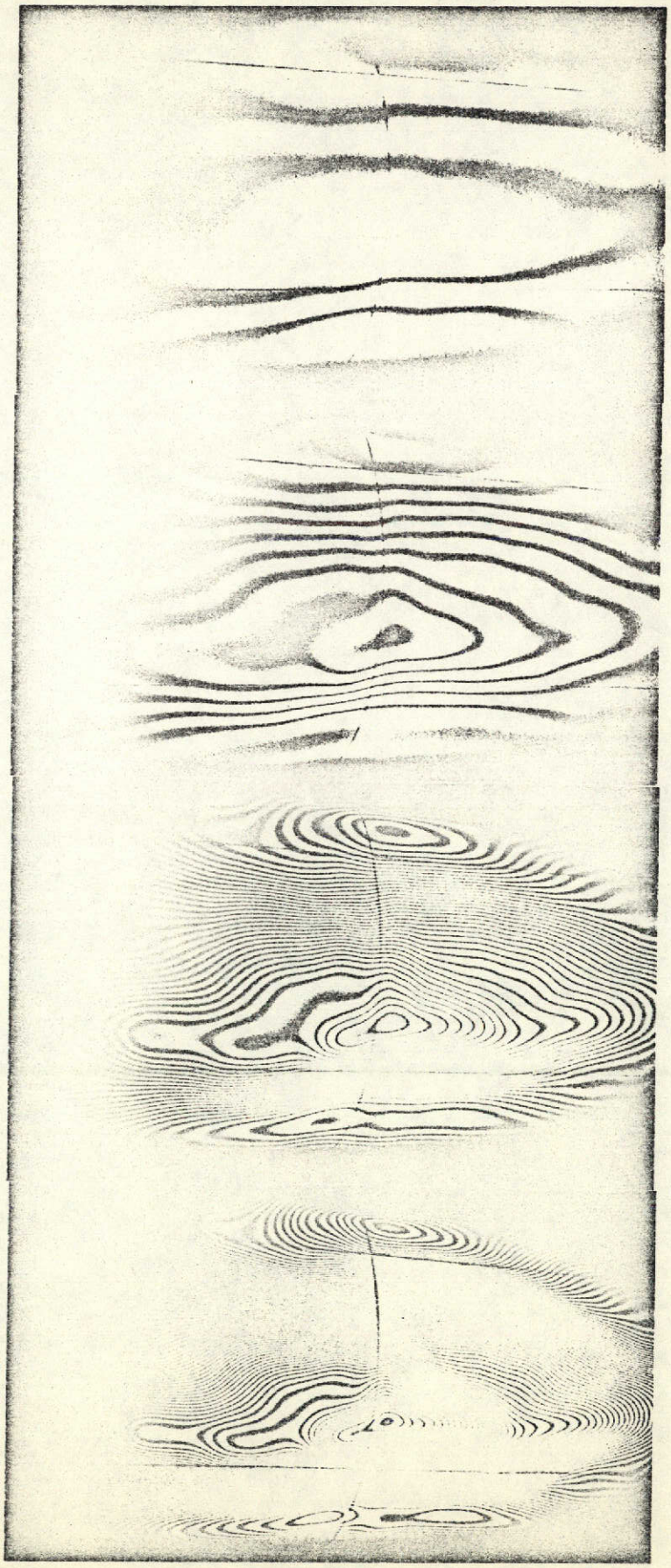

FIGURE

19

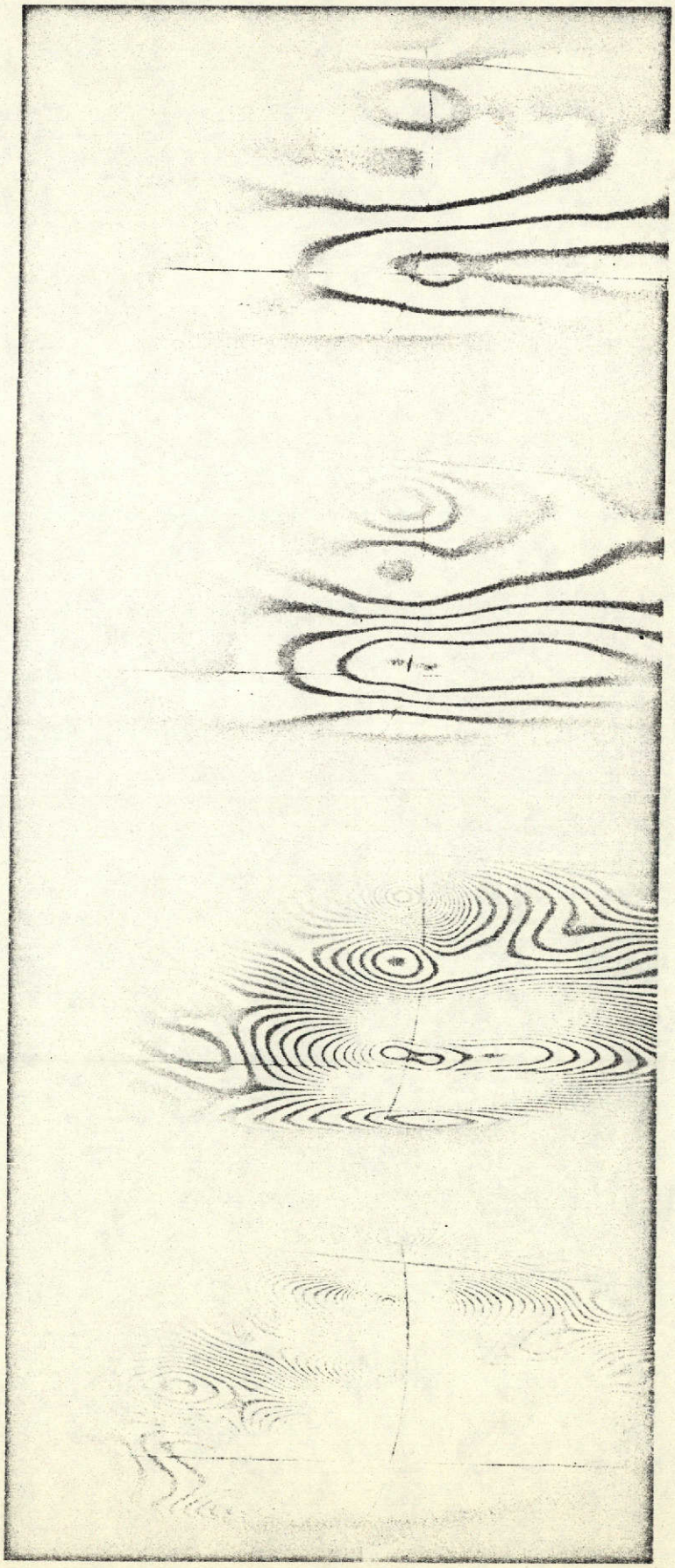

FIGURE
20

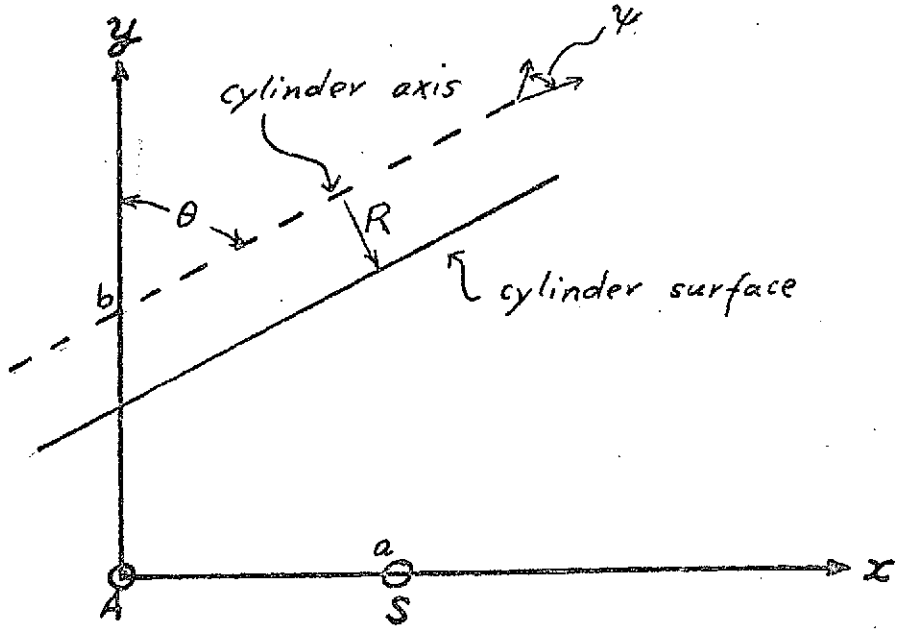

FIGURE 21